Geologic Interpretation of an Airborne Gamma Radiometric Survey, Salmon River Mountains, Idaho

A Thesis
Presented in Partial Fulfillment of the Requirements for the
Degree of Master of Science
with a
Major in Geology
in the
College of Graduate Studies
University of Idaho
by
Liam D. Knudsen

Approved by:
Major Professor: Karen S. Humes, Ph. D.
Committee Members: Reed S. Lewis, Ph. D; Robert W. Smith, Ph. D.
Department Administrator: Alistair M.S. Smith, Ph. D.

May 2023

Abstract

An airborne gamma radiation survey was recently published for a region of the Salmon River Mountains which hosts deposits of cobalt and rare earth elements, both of which are listed as critical minerals. The airborne gamma radiation survey was collected due to the prospect for undiscovered critical mineral deposits within the region.

Airborne gamma radiation surveys measure the concentrations of potassium, uranium, and thorium in the top 30 centimeters of the Earth's surface. Because individual rock lithologies typically have unique concentrations of potassium, uranium, and thorium, airborne gamma radiation data is used to delineate the distribution of geologic map units and to identify areas of anomalous gamma radiation signals, which may be related to alteration or mineralization.

Analyses of the survey were carried out to provide information for the improvement of the geologic framework and to identify areas where the gamma radiation data is anomalous for the mapped rock lithology. K-means clustering, principal component analysis, Kohonen self-organizing maps, and band ratios were used to analyze the airborne gamma radiation data. The clustering techniques were largely successful in delineating lithologies within the study area. Band ratios highlighted areas which may be altered. Through the clustering techniques, anomalous areas were identified, including both areas known to be mineral deposits and areas which warrant further investigation for the refinement of the geologic framework and for the possibility of mineralization.

Acknowledgments

First, I profoundly thank Dr. Reed Lewis of the Idaho Geological Survey for his tremendous guidance and support throughout this project. I thank University of Idaho faculty members Dr. Karen Humes for serving as major professor and Dr. Bob Smith for serving as a committee member. The direction, academic expertise, and feedback which they have provided is greatly appreciated. I thank Mr. Geoffrey Phelps of the U.S. Geological Survey for insight and suggestions provided at the start of this project. I thank Dr. JoAnn Holloway of the U.S. Geological Survey for her mentorship and advice. I thank all Idaho Geological Survey personnel involved in supporting this work and in creating the geologic data used for this project, namely Dr. Russell Burmester, Mr. Dave Stewart, Dr. Claudio Berti, and Dr. Nathan Hopkins. Lastly, I thank University of Idaho faculty Dr. Renee Love and Dr. Jerry Fairley for their advice during my time as a master's student.

Table of Contents

List of Tables

List of Figures

Chapter 1: Introduction

Critical minerals are essential for a variety of high-technology energy and military applications (Schulz et al., 2017). Critical minerals listed by the federal government on account of a combination of strategic or economic importance and supply chain insecurity include cobalt and the rare earth elements (U.S. Geological Survey, 2022). To enhance the supply of critical minerals, the Earth Mapping Initiative, which is a collaboration between the U.S. Geological Survey and state geological surveys, provides geologic, geochemical, and geophysical data to improve knowledge of the nation's geology and to identify areas that have potential to contain undiscovered critical mineral resources. The U.S. Geological Survey selects priority areas for mapping and data collection based on their potential to contain undiscovered critical mineral deposits (Day, 2019). One such area that was identified as potentially containing undiscovered critical mineral deposits was the Salmon River Mountains of Idaho. Within the Salmon River Mountains is the Idaho cobalt belt, which is a northwest-trending zone of cobalt mines and deposits, including Blackbird, Blackpine, Ram, and Iron Creek (Bookstrom, 2013). The area also contains several rare earth element properties, including the Diamond Creek deposit (Swallow, 2022).

In October of 2021, an airborne geophysical survey was carried out in the area (Figure 1.1) as part of the Earth Mapping Resource Initiative (Phelps, 2022). During the survey both magnetic and radiometric data were collected. Airborne radiometric data is sensitive to the concentration of potassium, effective concentrations of uranium and thorium, and the total counts of gamma radiation in the top 30 centimeters of the Earth's surface (Dickson and Scott, 1997). This sensitivity allows for differentiation of lithologic units, aiding geologic mapping efforts. Additionally, some mineralization processes are reflected by changes in radioelement concentration, such as increase in potassium concentration due to sericitization (Shives et al., 2000). The radiometric data published by Phelps (2022) provides interpolated concentrations of potassium, uranium, and thorium, and total counts of gamma radiation, as 40-meter grid cells.

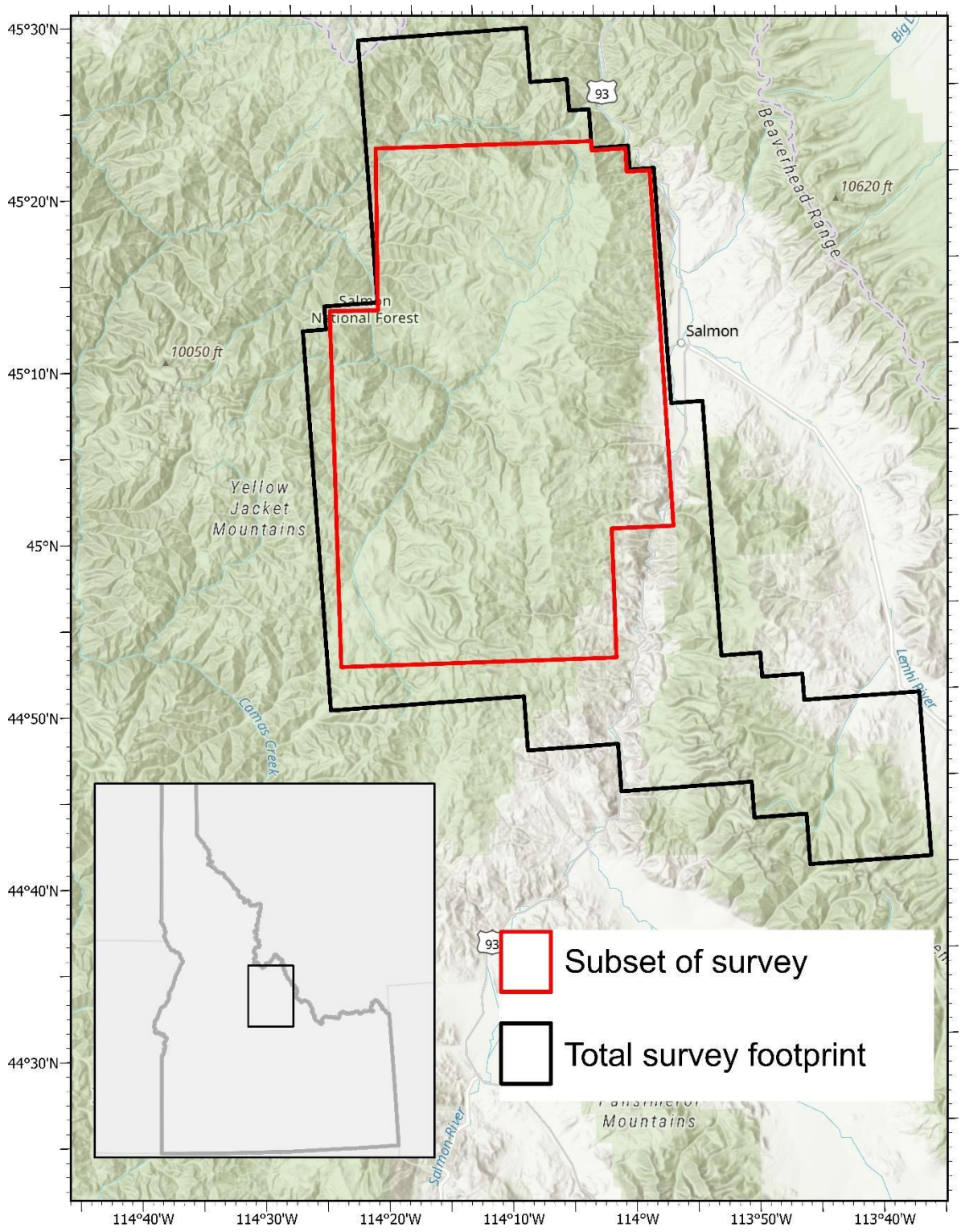

Figure 1.1 Footprint of the survey area and of the subset analyzed.

The objective of this study was to perform various analyses on a subset of the airborne radiometric survey to provide information to aid future geologic mapping efforts and to delineate focused target areas for mineral exploration. The subset of the survey (Figure 1.1) was limited to a contiguous area where the Idaho Geological Survey had previously carried out geologic mapping. Analyses techniques included k-means clustering, principal component analysis, Kohonen self-organizing maps, band ratios, and mean differencing. The results of the analyses were compared to compiled geologic mapping. Areas where radioelement concentrations differ from those expected based on the mapped lithologies were identified. These anomalous areas were further considered as areas where the geologic framework is incompletely understood and should be further investigated and as areas that may be candidates for mineral exploration activities.

Geological and Geophysical Background

The geology within the study area is diverse and structurally complex. Lithologies within the region include Mesoproterozoic metasedimentary units, Mesoproterozoic intrusive units, Cambrian and Ordovician intrusive igneous and metasedimentary units, Cretaceous intrusive units, Tertiary sediments and extrusive units, and Quaternary alluvium, colluvium, and glacial till. A generalized geologic map of the area is shown in Figure 1.2 and a correlation of map units within the study area is shown in Figure 1.3. A summary of map units is in Table 1.1. Regional-scale faults include the Coiner and Poison Creek faults. Geologic mapping began in the area in the 1910s and is still ongoing. Organizations that have mapped in the area include the Idaho Geological Survey, the U.S. Geological Survey, and numerous private mining companies (Umpleby, 1913; Anderson, 1947; Bennett, 1977; Connor and Evans, 1987; Evans and Green, 2003; and Lewis et al., 2022).

The oldest rocks in the area are of the Mesoproterozoic Lemhi subbasin of the Belt-Purcell Supergroup. From oldest to youngest, the major Belt Supergroup metasedimentary units within the area are the Lemhi Group (Ylg), Swauger Formation (Ys), the Lawson Creek Formation (Ylc), and the coarse siltite (Yac), banded siltite (Yab), and Lake Mountain (Yalm) members of the Apple Creek Formation (Burmester et al., 2016b). The Lemhi Group is primarily comprised of gray feldspathic quartzite, and lesser gray siltite and argillite (Lewis et al., 2022). Stratigraphically above the Lemhi Group is the Swauger Formation, which is a white or light orange mature quartzite typically low in feldspar (Lewis et al., 2021b). In different locations, the Swauger Formation is stratigraphically overlain by either the Lawson Creek Formation or the coarse siltite member of the Apple Creek Formation (Burmester et

al., 2016). The Lawson Creek Formation is a red to dark-gray thin-bedded quartzite with lesser siltite and argillite (Lewis et al., 2022). The coarse siltite member of the Apple Creek Formation is comprised of gray-green siltite and typically has a relatively high magnetite content (Lewis et al., 2021b). Conformably overlying the coarse siltite member is the banded siltite member of the Apple Creek Formation. Distinct to the banded siltite are graded couplets of white quartzite and siltite and dark-gray argillite, which give the unit its characteristic banding (Lewis et al., 2021b). Above the banded siltite is the Lake Mountain member of the Apple Creek Formation, which is a feldspathic quartzite with lesser siltite and argillite (Lewis et al., 2021b). During the Mesoproterozoic, the Belt Supergroup was folded and faulted and intruded by the Mesoproterozoic granite (Ygr) and mafic complex (Ymc) (Burmester et al, 2016). The Mesoproterozoic granite is a light-gray to pink granite which is commonly porphyritic with phenocrysts of microcline and plagioclase (Lewis et al., 2022). During the Cambrian and Ordovician, the Belt Supergroup and Mesoproterozoic granite were intruded by gabbro (Cgb), the Deep Creek syenitic complex (Csydc). and the Arnett Creek syenitic complex (OCsya) (Lewis et. al, 2022). During the Ordovician, the Kinnikinic Quartzite (Ok), which is a white vitreous quartzite, was unconformably deposited on Mesoproterozoic strata (Hansen and Pearson, 2016; Lewis et al., 2021b). The Kinnikinic Quartzite is overlain by the Saturday Mountain Formation (SOs), which is a dolomitic limestone (Hansen and Pearson, 2016; Lewis et al., 2021b). During the Cretaceous, intrusion of the Idaho batholith emplaced granite (Kg) and granodiorite (Kgd). Extensional faulting during the Tertiary allowed for deposition of sediments (Ts) and extrusion of the Challis Volcanic Group (Tcv) (Bennett, 1986). The Challis Volcanic Group is subdivided into many units, including rhyolite tuffs and mafic lavas.

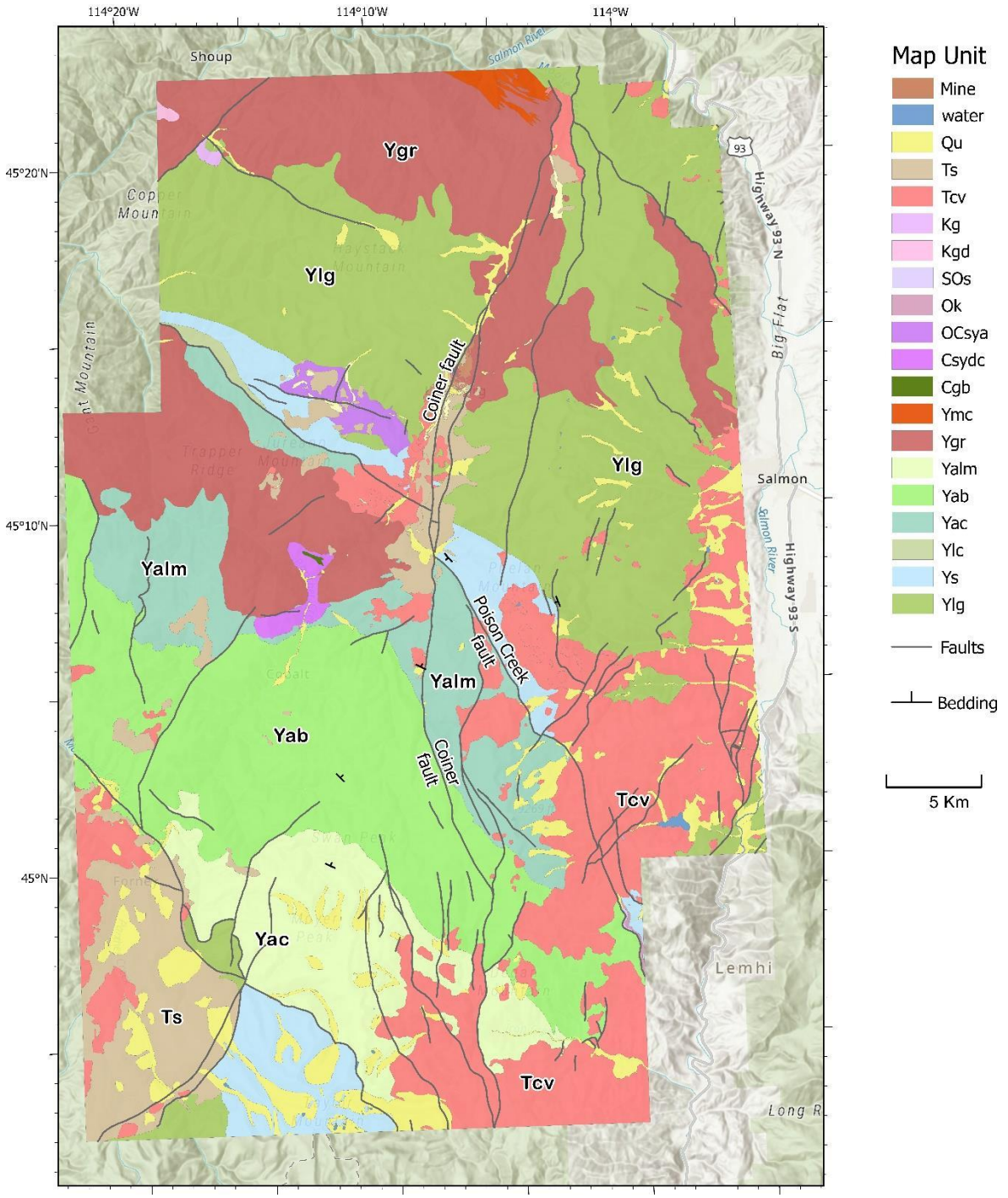

Figure 1.2 Compiled geologic map from both published and unpublished IGS mapping. Tertiary Challis Volcanics are presented undivided, as are all Quaternary units.

Table 1.1: General description of map units within the study area. From Lewis et al., 2022; Lewis et al., 2021b; Lewis et al., 2019; and Evans and Green, 2003.

Unit Symbol	**Unit Name**	**Lithologic Description**
Qu	Sedimentary deposits, undivided (Quaternary)	Clay- to boulder-size alluvium, landslides, and glacial till
Ts	Sedimentary deposits, undivided (Tertiary)	Gravel deposits, mudstones, sandstones, and cobble and boulder conglomerates
Tcv	Challis Volcanics, undivided (Tertiary)	Extrusive lithologies including rhyolite tuff, dacite tuffs and flows, and flows of andesite, trachyandesite, and basalt
Kg	Granite (Cretaceous)	Biotite-muscovite granite
Kgd	Granodiorite (Cretaceous)	Biotite granodiorite
SOs	Saturday Mountain Formation (Silurian-Ordovician)	Dolomitic limestone
Ok	Kinnikinic Quartzite (Ordovician)	Mature quartzite
OCsya	Arnett Creek syenitic complex (Ordovician to Cambrian?)	Mafic syenite, quartz monzonite, and leuco-syenogranite
Csydc	Deep Creek syenitic complex (Cambrian)	Alkali-feldspar syenite and alkali-feldspar granite
Cgb	Gabbro (Cambrian)	Hornblende-pyroxene gabbro and amphibolite
Ymc	Mafic complex (Mesoproterozoic)	Gabbro, diorite, and amphibolite
Ygr	Granite (Mesoproterozoic)	Granite with plagioclase phenocrysts and microcline megacrysts
Yalm	Lake Mountain member of the Apple Creek Formation (Mesoproterozoic)	Feldspathic quartzite with minor siltite and argillite

Table 1.1 cont'd

Yab	Banded siltite member of the Apple Creek Formation (Mesoproterozoic)	Couplets of quartzite/siltite and argillite with distinctive grading
Yac	Coarse siltite member of the Apple Creek Formation (Mesoproterozoic)	Siltite and quartzite with local mud cracks
Ylc	Lawson Creek member of the Apple Creek Formation (Mesoproterozoic)	Quartzite and siltite with minor argillite
Ys	Swauger Formation (Mesoproterozoic)	Mixed clean and locally feldspathic quartzite
Ylg	Lemhi Group (Mesoproterozoic)	Feldspathic quartzite with lesser siltite and argillite

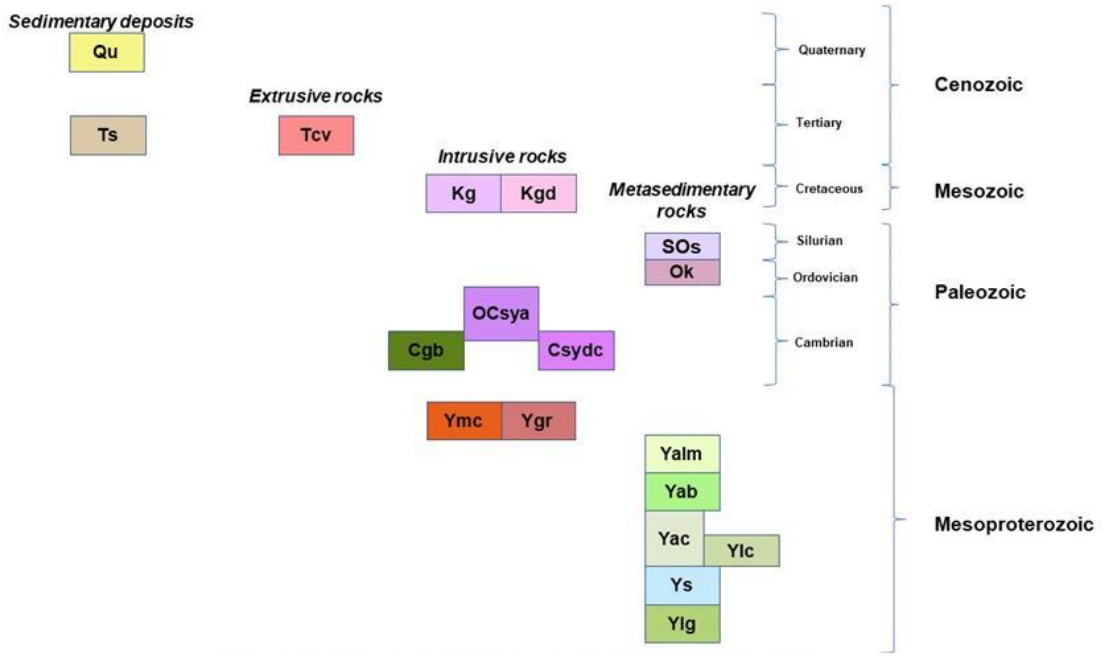

Figure 1.3 Correlation of map units within the study area. Not to scale. Modified from Lewis et al., (2021a), Lewis et al., (2021b), and Lewis et al., (2019).

Economic Geology Background

Historic mining for cobalt, copper, and gold has been conducted by multiple companies within the Idaho Cobalt Belt. Figure 1.4 below shows the locations of significant mines and mineral deposits within the study area and their associated commodities. Exploration and development of cobalt resources are presently underway by Electra Battery Materials Corporation at the Iron Creek deposit (Perron et al., 2023), and by Koba Resources Limited at the Blackpine deposit (Koba Resources Limited, 2023). At Jervois Global's Idaho Cobalt Operations, which is currently the largest NI 43-101-compliant cobalt resource in the United States, final mine construction was recently suspended but exploration drilling is still ongoing (Crocker, 2023). Several rare-earth element properties are currently in the exploration and development phases, including Idaho Strategic Resources, Inc.'s Diamond Creek project (Swallow, 2022). In addition to cobalt and rare earth element deposits, the area hosts a large past-producing gold mine, Revival Gold's Beartrack Mine, which is currently in renewed exploration (Revival Gold, 2020). The area also contains historic hard-rock and placer gold mines, along with rare-earth element, uranium, niobium, and tin prospects (Idaho Geological Survey Mines and Prospects Database).

The Blackbird, Blackpine, and Ram deposits of the Blackbird Mining District are classified as Co-Cu-Au deposits within metasedimentary rocks (Bookstrom, 2016). At each of the deposits of the Blackbird Mining District the host rock is the banded siltite of the Apple Creek Formation (Bookstrom, 2016). The age and origin of the cobalt mineralization is a contentious subject, for which numerous hypotheses have been proposed, including Precambrian submarine-exhalative, Cretaceous thrust-related, epigenetic iron oxide copper-gold, and Mesoproterozoic magmatic-hydrothermal (Nash and Hahn, 1989; Lund, 2011; Slack, 2012; Bookstrom, 2016). The Diamond Creek rare earth element deposit is primarily hosted in the Lemhi Group immediately north of the contact with Mesoproterozoic granite and to a lesser extent within the granite. The mineralization is within monazite and rare-earth element bearing veins (Staatz et al., 1979; Idaho Strategic Resources, 2023). At the Beartrack mine, gold mineralization is hosted in veins within the Lemhi Group and the Mesoproterozoic granite. Mineralization is dated as Cretaceous (Steve Priesmeyer, written communication in Lewis et al., 2022). The deposit is a mesothermal system along the Coiner fault (Bissonnette and Kim, 2022; Lewis et al., 2022).

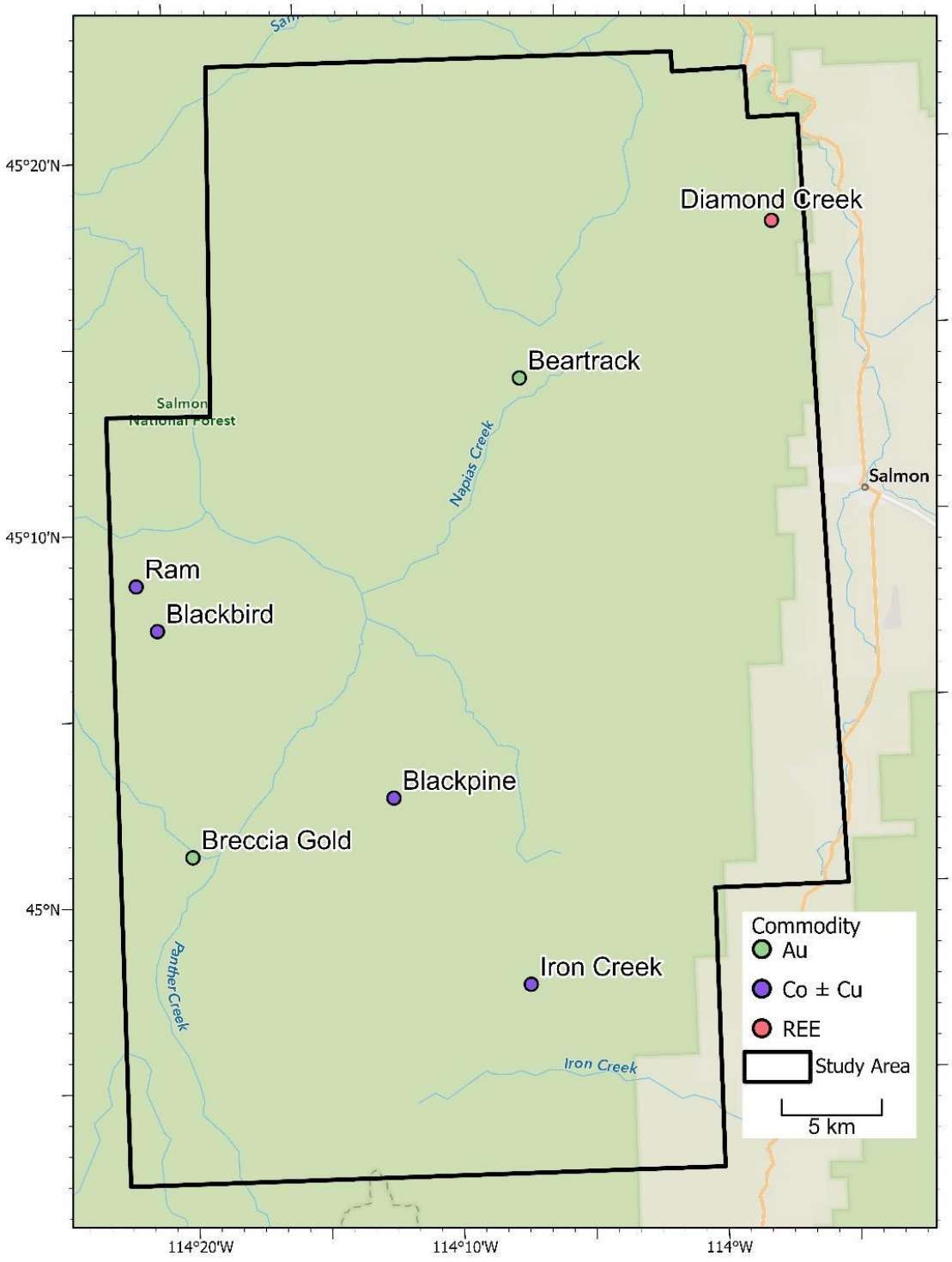

Figure 1.4 Locations of mines and mineral deposits in the study area discussed in the text.

Literature Review - Outcomes

Remote Predictive Mapping

Many researchers have applied statistical analyses on airborne gamma radiometric data to create remote predictive geologic maps or to refine existing geologic mapping. Remote predictive maps leverage remotely sensed data to inform future geologic mapping efforts and are especially useful in areas where field mapping is impaired by logistical difficulties, such as thick vegetative cover, remoteness, and rugged terrain (Harris et al., 1987). Harris et al. (1987) applied principal component analysis to airborne radiometric and magnetic data for predictive geologic mapping in Nova Scotia and Manitoba, Canada. The combination of data through principal component analysis allowed the multiple dimensions of potassium, uranium, and thorium concentrations, total field magnetics, and the magnetic vertical gradient to be displayed as a color composite image, which was used for lithologic discrimination. The authors found that principal component analysis effectively combined the geophysical data and allowed for separation of lithologic units. Weihermann et al. (2020) used the simple linear iterative clustering k-means algorithm to automatically map geologic units. The effectiveness of the clustering was evaluated by visually comparing clustering results to compiled geologic mapping. The authors found that the clusters corresponded well with the mapped geology and that some clusters reflected variation within geologic units. Carneiro et al. (2012) applied Kohonen self-organizing maps to cluster airborne radiometric and magnetic data in the Brazilian Amazon for the purpose of creating a predictive geologic map. The researchers evaluated the results of the self-organizing map through the comparison of clusters with the associated rock lithologies, which were determined through field sampling, petrography, and geochemical analysis, and found that the self-organizing map produced clusters spatially related to the rock lithologies. Carter-McAuslan and Farquharson (2021) clustered various combinations of airborne radiometric, magnetic, and gravity data using a self-organizing map. The best matching units determined by the self-organizing map were further clustered through k-means clustering to generate a predictive geologic map. The results of the self-organizing map and k-means clustering of the self-organizing map for each combination of the data were visually compared to compiled geologic mapping. The authors found that k-means clustering of the self-organizing map results created more accurately reflected the geology than the results of the self-organizing map alone.

Although many of the studies described above incorporated both gamma radiometric and magnetic data into clustering and principal component analysis, this approach requires assumptions which are not valid within the study area. Airborne magnetic surveys have much greater depth sensitivity than airborne gamma radiometric surveys (Dickson and Scott, 1997). As a result, if the rocks are of a different type at the depth measured by the magnetic data than at the depth measured by the radiometric data, the magnetic and gamma data generated from the airborne survey would reflect different signatures. Accordingly, clustering techniques or principal component analysis would be invalidly integrating dimensions which are a measure of different populations. The necessary geologic assumption that would allow for the magnetic and radiometric data to be integrated without combining measurements of different populations is that the rocks are homogenous from the depth measured by the radiometric survey to the depth measured by the magnetic survey. Because many of the rock units have moderate dips, the assumption is not valid for this study area, and the analyses within uses only the gamma radiometric survey.

Mineral Deposits

Analyses of airborne gamma radiometric data have been applied to discover and study mineral deposits. Wang et al. (2023) investigated an area of anomalously high thorium values in an airborne radiometric data survey, which was collected as part of the Earth Mapping Resources Initiative, and subsequently discovered a rare earth element–niobium–zircon occurrence. The thorium anomaly was investigated through ground traverses with a handheld gamma-ray spectrometer and geochemical analysis of rock samples. The field investigation confirmed the presence of a previously unknown rare earth element–niobium-zircon occurrence. In addition to identifying areas of anomalously high concentrations, statistical techniques such as principal component analysis have been applied to airborne radiometric data for mineral deposit exploration. Ranjbar et al. (2001) applied principal component analysis to a multidimensional data set to identify hydrothermally altered areas within the Darrehzar porphyry copper deposit in Iran. Data used by the authors for the principal component analysis included gamma spectroscopy, magnetic intensity, induced polarization, resistivity, and kriged rock and soil geochemical samples. Two areas identified through the principal component analysis were subsequently investigated in the field, one of which was determined to be a porphyry copper deposit of economic grade.

Another technique for the analysis of gamma radiation data is the application of band ratios, which represent the ratio between multiple radioelements. Shives et al. (1995) discuss case

histories regarding the application of the thorium to potassium band ratio to identify potassic alteration related to various types of mineralization, including porphyry Au-Cu-Mo, volcanic massive sulfide, and polymetallic magmatic-hydrothermal. As thorium is typically less mobile than potassium, areas of thorium to potassium band ratio lows, relative to normal lithologic concentrations, may represent hydrothermal potassic alteration, that, in the instances of the case studies, is related to mineralization. One case study discussed by Shives et al. (1995) was the discovery of the Sue-Dianne polymetallic magmatic-hydrothermal deposit near Lou Lake, Northwest Territories, Canada. The Sue-Dianne copper-uranium deposit was discovered through the investigation of a uranium to thorium band ratio anomaly (Charbonneau, 1988). Drilling in the location of the uranium to thorium anomaly indicated significant copper and uranium resources. In addition to the ratio between two elements, the relationship between the three radioelements has been applied in the search for mineral deposits. The Effimov factor, which represents the concentration of potassium multiplied by the uranium to thorium ratio, was used by Gnojek and Prichystal (1985) to discover a previously unknown region of lead-zinc mineralization in Czechoslovakia. The authors carried out ground verification on an area identified by the Effimov factor as a potassium high. Ground verification consisted of geochemical sampling and geophysical investigation, including induced polarization, resistivity, and magnetic surveys. The results of the ground investigation motivated a drilling program that intersected a previously unknown polymetallic mineral deposit.

Chapter 2: Methodology

Average Radioelement Concentrations

To develop an understanding of the average radioelement concentrations of major units within the study area, in situ measurements were taken using a Mount Sopris RS-125 handheld gamma-ray spectrometer by the author under direction of Idaho Geological Survey personnel (unpublished). At each outcrop, multiple measurements were taken for 60 seconds each. Measurements were taken on surfaces where the outcrop surface was flat.

Preprocessing

Radiometric

Each of the three radiometric rasters from Phelps (2022) were cropped to the extent of the study area. The original projection of the radiometric data (WGS 1984 UTM Zone 11) was preserved, and no transformations were performed. “No Data” (NA) values present in either the potassium, effective uranium, or effective thorium rasters were masked across all three rasters to allow for further statistical analyses.

Geology

Published and unpublished geologic mapping were compiled to provide geologic mapping coverage across the entire study area. GIS-format 1:24,000-scale geologic map quadrangles published by the Idaho Geological Survey were merged to create coherent geologic coverage of the area. Published maps that were merged, including from internal Idaho Geological Survey GIS databases, were Bird Creek (Burmester et al., 2012), Cobalt (Lewis et al., 2021a), Degan Mountain (Lewis et al., 2021b), Taylor Mountain (Stewart et al., 2021), Jureano Mountain (Lewis et al., 2022), Lake Mountain (in review), Leesburg (Lewis et al., 2022), Salmon (Lewis et al., 2012), and Williams Lake (Lewis et al., 2013). Unpublished geologic mapping carried out by Idaho Geological Survey personnel was provided by Dr. Reed Lewis. For some quadrangles field maps were scanned and heads-up digitized. Unpublished 1:24,000-scale maps that were digitized were Blackbird Creek, Gant Ridge, Gant Mountain, Napoleon Hill, Opal Lake, Pine Creek Rapids, and Pine Creek Ridge. The projected coordinate system of NAD 1927 State Plane Idaho Central was maintained for the digitizing and compilation process.

Color composites

The potassium, uranium, and thorium raster datasets were cropped to the outline of the study area in ArcGIS Pro (Esri Inc., 2022). The raster datasets were imported into RStudio

(R Core Team, 2022), and NA values present in any of the three rasters were masked. The three rasters were stacked as a single multiband raster and exported. The multiband raster was then visualized in ArcGIS Pro as a RGB image with potassium represented as red, thorium as green, and uranium as blue.

Bivariate plots

Bivariate plots for each permutation of the radioelements were created. The map unit polygons were converted to raster data with the same cell size (40m) and snapped to the same cell corner as the radiometric rasters. The new raster was transformed from NAD 1927 State Plane Idaho Central to WGS 1984 UTM Zone 11. The raster representing the geologic map units was imported into RStudio, and a RasterStack object with the four bands of potassium, thorium, uranium, and geologic map unit was created. Cells representing four major Belt units in the region, the Swauger Formation and the banded siltite, coarse siltite, and Lake Mountain members of the Apple Creek Formation, were selected. From this selection, the RStudio ‘pairs’ function was applied to create a plot matrix of each combination of the radioelement dimensions.

Principal component analysis

To perform principal component analysis, the new copies of cropped and masked potassium, uranium, and thorium rasters were loaded in RStudio. The data were centered and z-scaled using the ‘scale’ function of the base RStudio package. Using the ‘rasterPCA’ function of the ‘raster’ base package, principal component analysis was performed on the three dimensions. To ascertain the importance of each principal component, the individual and cumulative proportion of variance for each principal component was determined, and to establish the correlation of the original variables with the principal components the loadings were calculated. The resulting principal components were exported as a raster image representing the first principal component. The raster was visualized in ArcGIS Pro as a stretched image representing the first principal component.

K-means

The cropped and masked potassium, uranium, and thorium rasters were loaded in RStudio. The three rasters were stacked into a multiband raster. The data were centered and z-scaled using the ‘scale’ function of the base RStudio package. The scaled and centered RasterStack was converted into an aspatial data frame object. The within-cluster sum of squares was iteratively calculated for one to fifteen clusters. The within-cluster sum of

squares represents the variability of data within each cluster. Typically, increasing the amount of k clusters yields diminishing returns of minimized variability within each cluster. Additionally, using more clusters may result in greater difficulty in interpretation. One technique to ascertain the appropriate number of clusters is the elbow method, in which the approximate asymptote of within-cluster sum of squares is determined. After estimating the ideal number of clusters as seven, K-means classification was performed using the ‘kmeans’ function of the ‘stats’ package. The Lloyd K-means algorithm was used. The resultant output classification was written to the cropped and masked multiband raster as a new band such that each cell was assigned an integer representing the cluster the cell was classified as. The classified raster was exported and visualized in ArcGIS Pro with each integer symbolized as a unique color.

Kohonen self-organizing maps

To create the self-organizing map, the three cropped and masked copies of the radiometric rasters were loaded into RStudio. The three rasters were stacked into a RasterStack object and coerced into a data frame object. Using the ‘scale’ function of the ‘base’ RStudio package, the data frame was converted into a centered and z-scaled matrix. Using the ‘som’ function of the ‘kohonen’ package, a self-organizing map was created with a grid of seven by one nodes. The self-organizing map was plotted with the average concentrations of the radioelements for each node represented as radii. The node that each data point was assigned to was written to the original data frame. The data frame was converted into a raster. The raster was exported and visualized in ArcGIS Pro with the integer value of each of the seven nodes symbolized as a unique color. Because of the topological relationship of self-organizing maps, a continuous color ramp was used to symbolize the integers.

Combinations of techniques

Whereas the self-organizing map described above clustered the data using the potassium, uranium, and thorium dimensions, a similar technique can be applied to cluster the principal components. As each successive principal component represents decreasing variability, only the first principal component was clustered.

Band ratios

Potassium/Thorium

The cropped and masked copies of the potassium and thorium rasters were loaded into RStudio. A raster representing the ratio of potassium to thorium was created by dividing the

potassium raster by the thorium raster. The new raster was exported and visualized in ArcGIS Pro as a stretched image.

Effimov factor

The cropped and masked copies of the potassium, uranium, and thorium rasters were loaded into RStudio. Using the expression “Potassium × Uranium ÷ Thorium”, the Effimov factor was calculated for each grid cell. The new raster was exported and visualized in ArcGIS Pro as a stretched image.

Chapter 3: Results and Discussion

Average Radioelement Concentrations

The average concentrations of potassium, uranium, and thorium as measured by the handheld gamma-ray spectrometer are presented below in Table 3.1. Individual Tertiary Challis volcanic units are presented as Challis volcanics, undivided. The igneous extrusive Challis volcanics and intrusive Mesoproterozoic granite have relatively high concentrations of thorium and uranium. The Belt Supergroup units share roughly similar radioelement concentrations, except for the Swauger Formation, which has low concentrations of all three radioelements.

Table 3.1: Average handheld gamma radiation measurements for major units within the study area.

Lithology	Mean K (%)	Mean U (ppm)	Mean Th (ppm)
Challis volcanics (Tcv)	4.42	7.01	28.1
Mesoproterozoic granite (Ygr)	6.13	6.24	43.9
Lake Mountain (Yalm)	4.48	4.96	19.0
Banded siltite (Yab)	4.20	5.20	18.4
Coarse siltite (Yac)	3.31	5.02	15.6
Swauger Formation (Ys)	1.82	2.45	4.55
Lemhi Group (Ylg)	3.55	4.02	14.0

Similarly, the distributions of potassium, uranium, and thorium concentrations for the major units within the study area are presented as boxplots below in Figures 3.1-3.3.

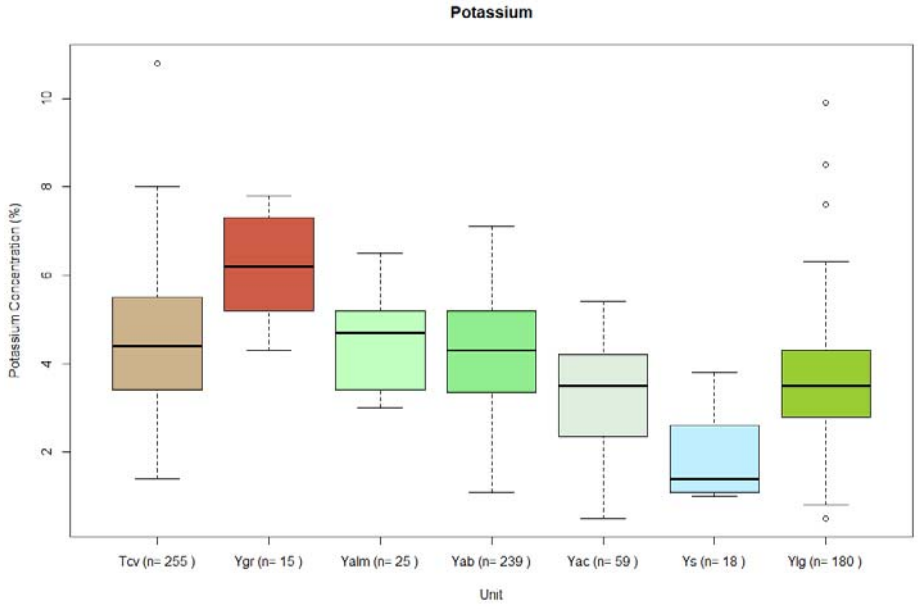

Figure 3.1 Boxplot of handheld gamma-ray spectrometer measurements of potassium concentrations.

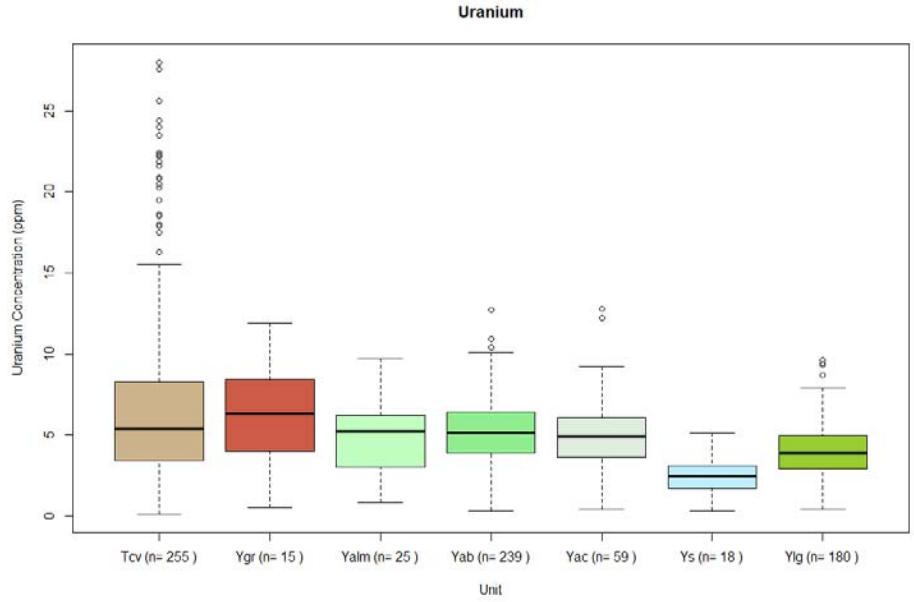

Figure 3.2 Boxplot of handheld gamma-ray spectrometer measurements of uranium concentrations.

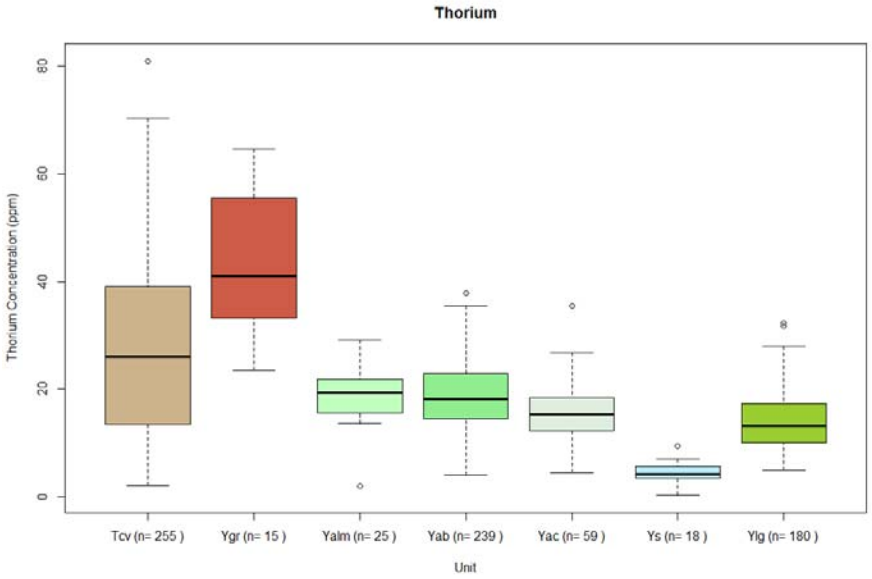

Figure 3.3 Boxplot of handheld gamma-ray spectrometer measurements of thorium concentrations.

Bivariate plots

The bivariate plot matrices of airborne gamma radiation for selected geologic units are presented below in Figures 3.4 and 3.5. The two plot matrices represent the same data – in the second image points are plotted in reverse order, so that units obscured in the first image can be seen. As an example of how to read these plots, the lower left plot in the matrices represents potassium concentration on the x-axis and thorium concentration on the y-axis. Conversely, the x-axis of the upper right plot is thorium, and the y-axis is potassium.

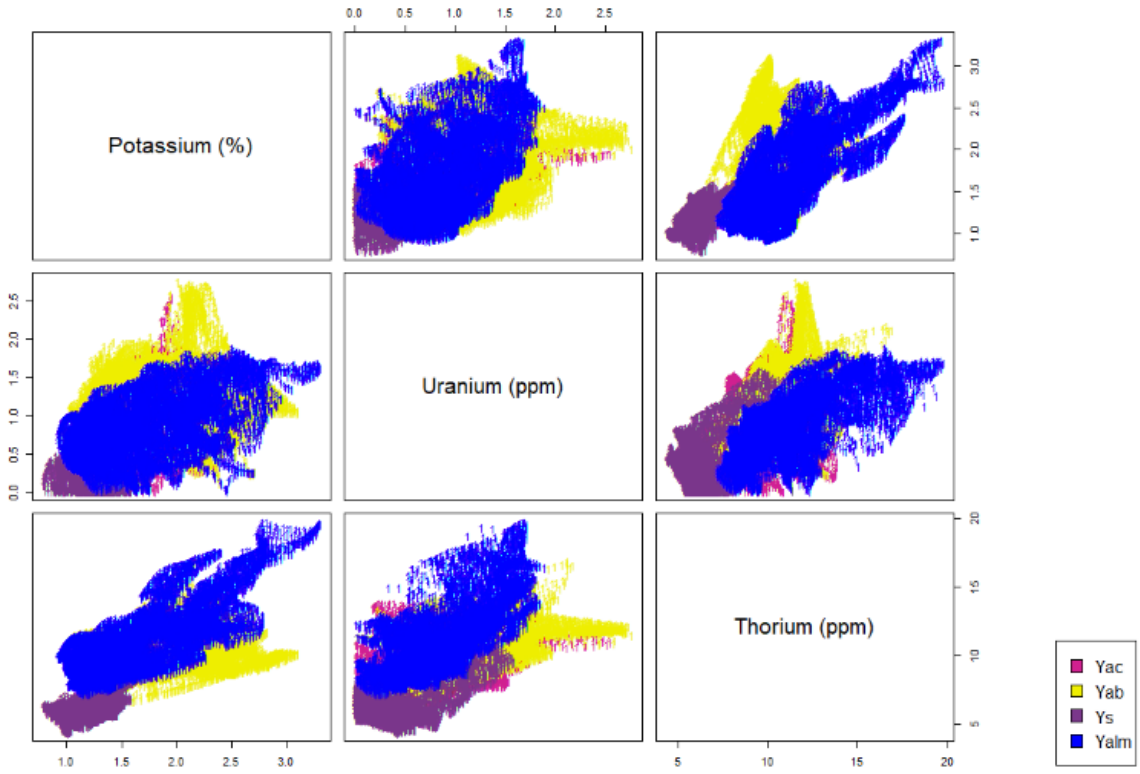

Figure 3.4 Bivariate plot matrix of airborne gamma radiation concentration for selected Belt units within the Degan, Taylor Mountain, and Cobalt quadrangles.

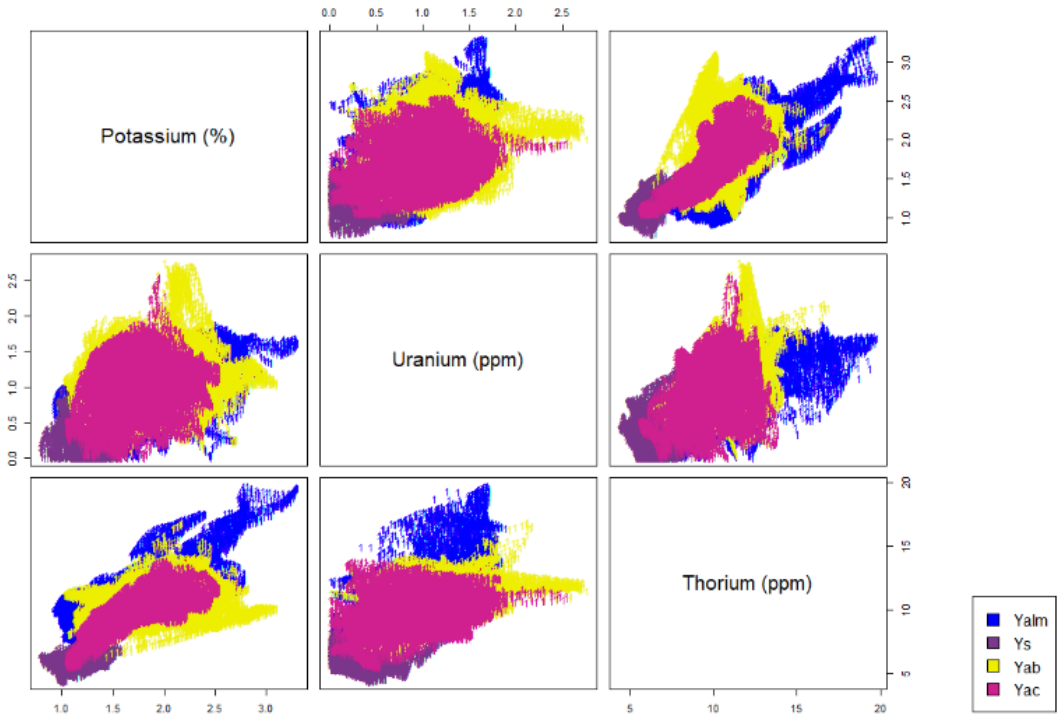

Figure 3.5 Reverse order bivariate plot matrix of airborne gamma radiation concentrations for selected Belt units within the Degan, Taylor Mountain, and Cobalt quadrangles.

Because of the similarity of the various siltite, argillite, and quartzite units of the Belt Supergroup, there is much overlap in radiometric space between the four units shown above. The Swauger Formation consistently appears in the lower left of the plots due to low concentrations of potassium, uranium, and thorium. However, the Lemhi Group, coarse siltite, and banded siltite have largely similar radioelement concentrations. As a result, the ability to discriminate between Belt units by clustering the radiometric data is limited.

Color composites

Several geologic features are immediately apparent in the RGB color composite image. Figure 3.6 demonstrates the RGB color composite of potassium, uranium, and thorium with the addition of geologic contacts and selected mines. Toward the southwest corner of the study area a dark purple to black region can be seen (Figure 3.6, location one). In this RGB color space, black represents areas where the concentrations of radioelements are low. Low concentrations of the radioelements are characteristic of the Swauger Formation (Figures 3.3-3.5). In addition to the Swauger Formation, Tertiary sediments of Swauger provenance are mapped within this region. Similarly, the zone of black to dark purple colors in the center of the study area is mapped as Swauger Formation (Figure 3.6, location two). Along the eastern boundary of the study area two light yellow/white bodies can be seen. The more

southern ellipsoidal feature (Figure 3.6, location three) encompasses multiple tuffaceous units of the Challis volcanics, which are typically high in potassium and thorium (Lewis and Myers, 2012). The more northern elongated body (Figure 3.6, location four) represents Mesoproterozoic granite (Ygr). The bright white/light blue body on the western margin of the Figure (Figure 3.6, location five) is an area of tuff of Castle Rock. In the northern region of the image (Figure 3.6, location six), the contact between Ygr and Ylg can be seen in the contrast of tan, light yellow, and light green colors with dark green and orange colors.

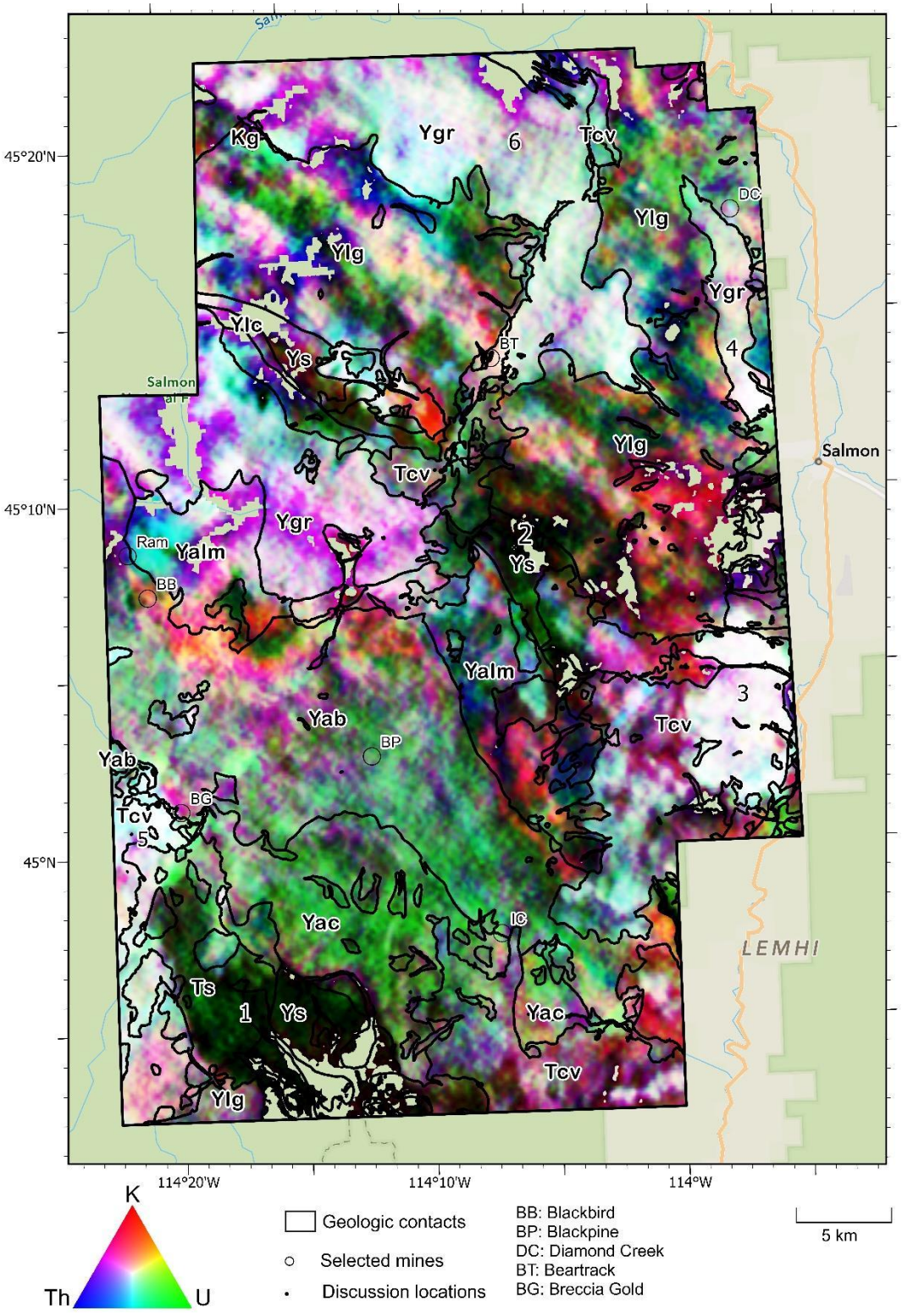

Figure 3.6 RGB color composite image of airborne gamma radiation measured concentrations of potassium, uranium, and thorium within the study area.

Principal component analysis

For the study area, high values in the first principal component typically represent intrusive and extrusive igneous geologic units and low values typically represent metasedimentary units. The output of the principal component analysis is effective at distinguishing between igneous rocks and metasedimentary rocks. The increasing proportion of variance accounted for in each principal component is provided in Table 3.2. Table 3.3 provides the loadings of the original variables on each of the principal components. The first principal component is correlated similarly with each of the original variables. The second principal component is correlated well with potassium and uranium concentrations and is not correlated well with thorium concentrations. The third principal component is primarily correlated with thorium concentrations. In Figure 3.7 the first principal component is shown as a stretched image, with the addition of the mapped geologic contacts and selected mine locations. Locations one and two in Figure 3.7 demonstrate the differentiation between Mesoproterozoic granite and Lemhi Group through the first principal component. Similarly, the first principal component can be effectively used to distinguish between the locations of extrusive igneous and metasedimentary units, as is demonstrated at locations three and four. Additionally, the Swauger Formation, due to characteristically low concentrations of potassium, uranium, and thorium, is separated in principal component space, as can be seen at location five. However, separation of the remaining Belt Supergroup units is less successful. For example, the contact between the coarse siltite and banded siltite (location six) is not delineated well by the principal component analysis, due to major overlap of the Belt units in radiometric space. The first principal component values representative of the extrusive and intrusive igneous map units are largely equivalent, as can be seen by comparing the first principal component in areas of Mesoproterozoic granite to areas of Tertiary Challis Volcanics.

There are multiple areas for which the principal component values resemble values typically representative of the igneous map units, but that are well constrained by field mapping by the Idaho Geological Survey as Belt Supergroup. One example is the Diamond Creek rare earth element deposit (labelled as ‘DC’ in Figure 3.7), which appears as two small bull’s-eyes of high first principal component values within the Lemhi Group. An additional example is location seven, which will be discussed later in the text in further detail.

Table 3.2: Proportion of variance for each principal component.

	PC1	PC2	PC3
Proportion of Variance	76.77%	15.98%	7.24%
Cumulative Proportion	76.77%	92.75%	100%

Table 3.3: Loadings of original variables on the principal components.

Loadings	PC1	PC2	PC3
Potassium	0.565	0.668	0.484
Uranium	0.553	-0.742	0.379
Thorium	0.612	0.054	-0.789

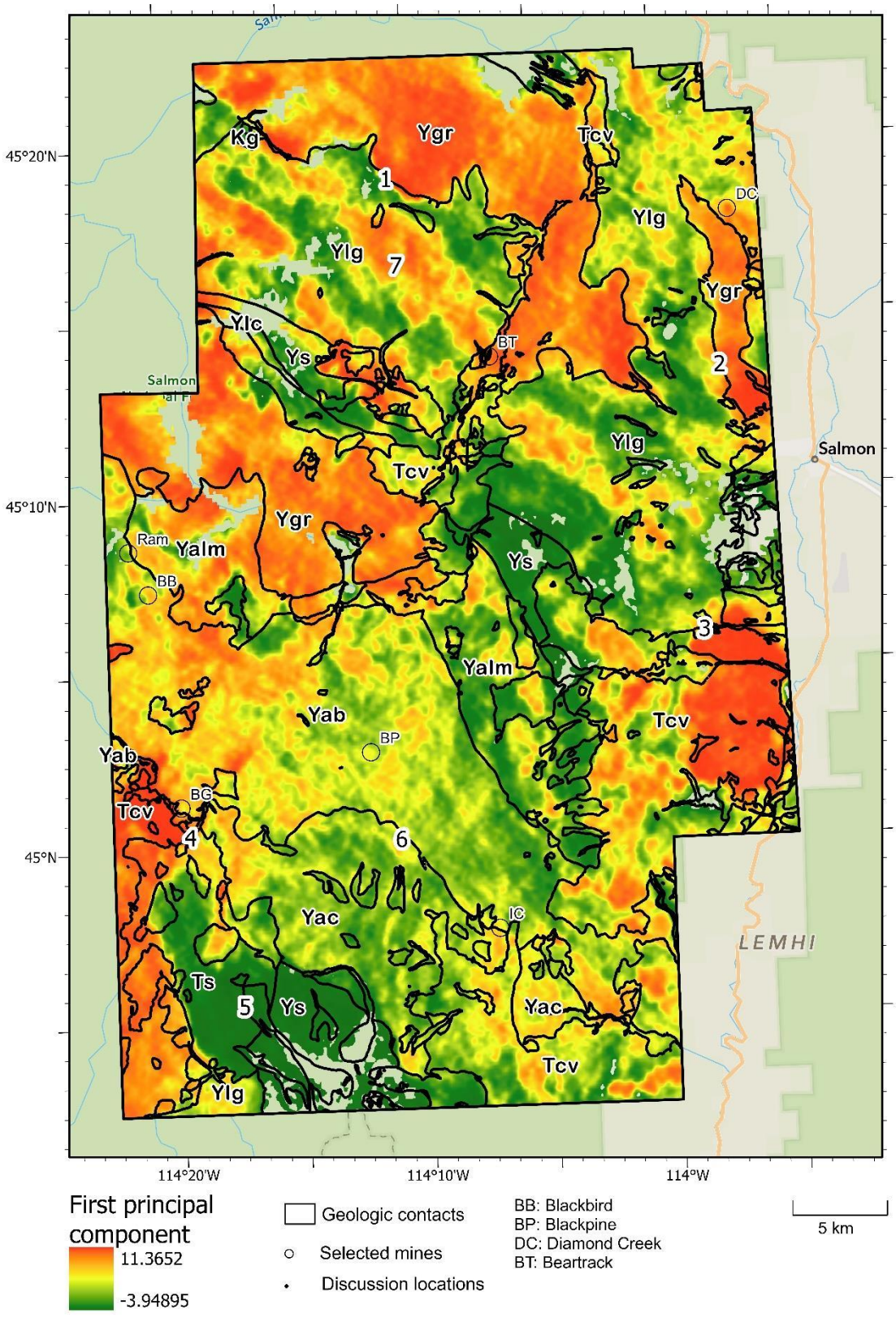

Figure 3.7 First principal component plotted as a histogram equalized stretched image.

K-means clustering

The k-means clustering is effective at separating the igneous and metasedimentary rocks within the study area. Figure 3.8 below shows the spatial distribution of the k-means clusters with the addition of the geologic contacts and locations of selected mines. Clusters four, six, and seven primarily represent Belt Supergroup units. Clusters one, two, and five primarily represent extrusive and intrusive igneous rocks. Cluster three encompasses both metasedimentary and igneous rocks. Due to large radiometric contrast, contacts between the Mesoproterozoic granite and Belt Supergroup units are delineated well, as can be seen in Figure 3.8 at locations one and two. Similarly, contacts between the Tertiary Challis Volcanics and Belt Supergroup units can be seen in the clustering analysis, such as at locations three and four. The extent of the Swauger Formation, including Tertiary sediments of Swauger provenance, is delineated well at the southern end of the study area by cluster four (location five). However, due to radiometric similarities between non-Swauger Belt Supergroup units, the clustering analysis largely does not capture stratigraphic contacts. For example, there is no apparent change of clusters at the contact of the banded siltite and coarse siltite at location six.

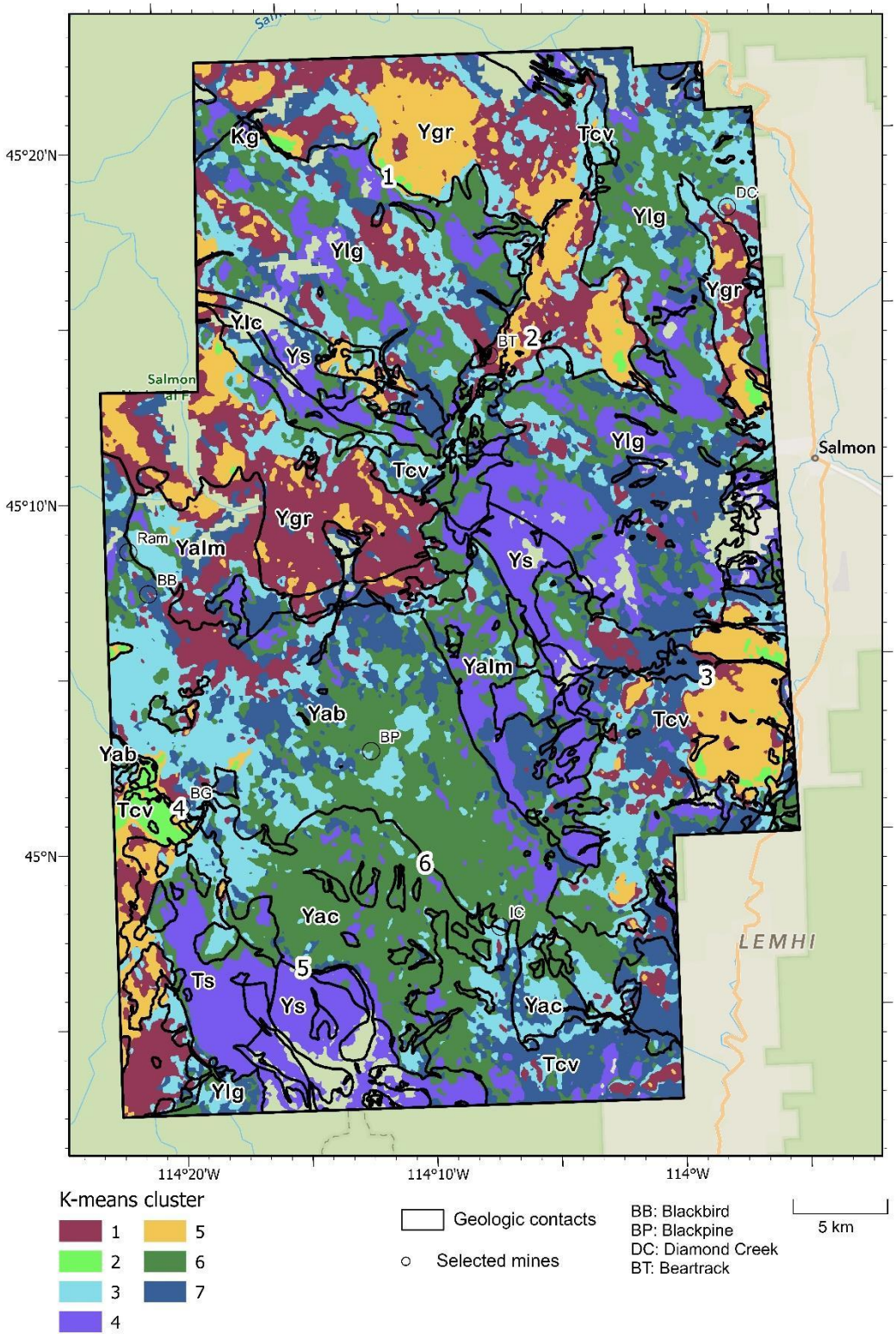

Figure 3.8 Resultant image from k-means clustering with seven clusters.

Kohonen self-organizing maps

The spatial output of the results of the self-organizing map closely resemble that of the k-means clustering. In Figure 3.9, the radii of each dimension represent the average abundance of the various radioelements within each node. The resultant clustered image from the self-organizing map (Figure 3.10) is presented below. Within the study, a Kohonen self-organizing map of the radiometric data is largely successful at distinguishing the metasedimentary rocks from intrusive and extrusive rocks. The change between self-organizing map clusters frequently matches the location of mapped contacts between the Mesoproterozoic granite and Belt Supergroup units, such as the Lemhi Group. Examples of this can be seen at locations one and two in Figure 3.10. Similarly, the results of the self-organizing map successfully capture many of the contacts between the Challis volcanic and Belt Supergroup units, as can be seen at locations three and four. For the most part, the radiometric difference is not great enough between Belt Supergroup units to differentiate them through the self-organizing map algorithm, except for separating the Swauger Formation (location five). The output of the Kohonen self-organizing map largely groups the intrusive Mesoproterozoic granite and extrusive Challis volcanics into the same clusters. In some places, the output organizes Belt units into classifications typically representative of the igneous intrusive and extrusive units. Regional-scale examples of this can be seen in the swaths of clusters six and seven in the northwest corner of the study area (location six) and the region south of the Blackbird Mine (location seven). Field-based investigation is necessary to understand the process(es) responsible for these swaths.

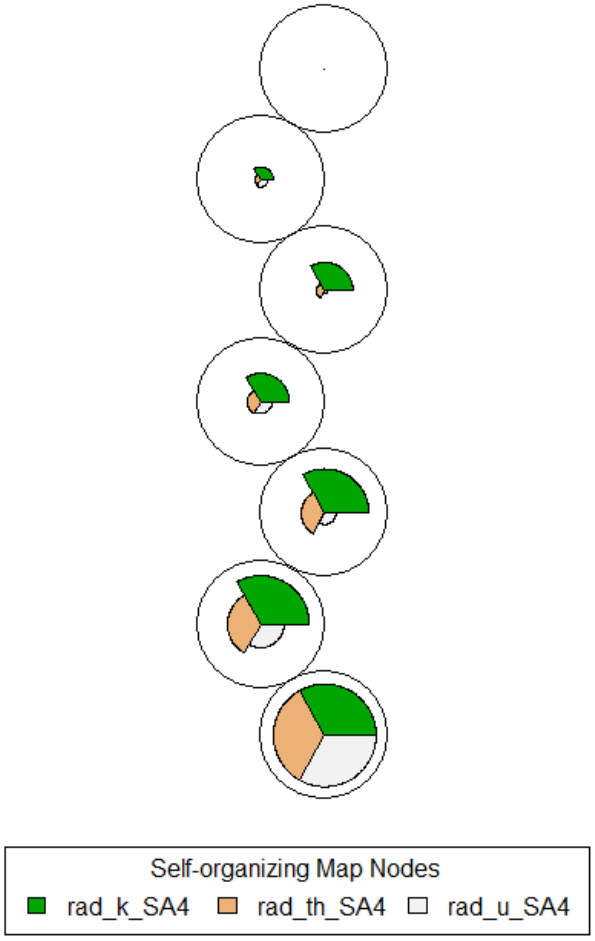

Figure 3.9 Average relative concentrations of potassium, uranium, and thorium for each self-organizing map node.

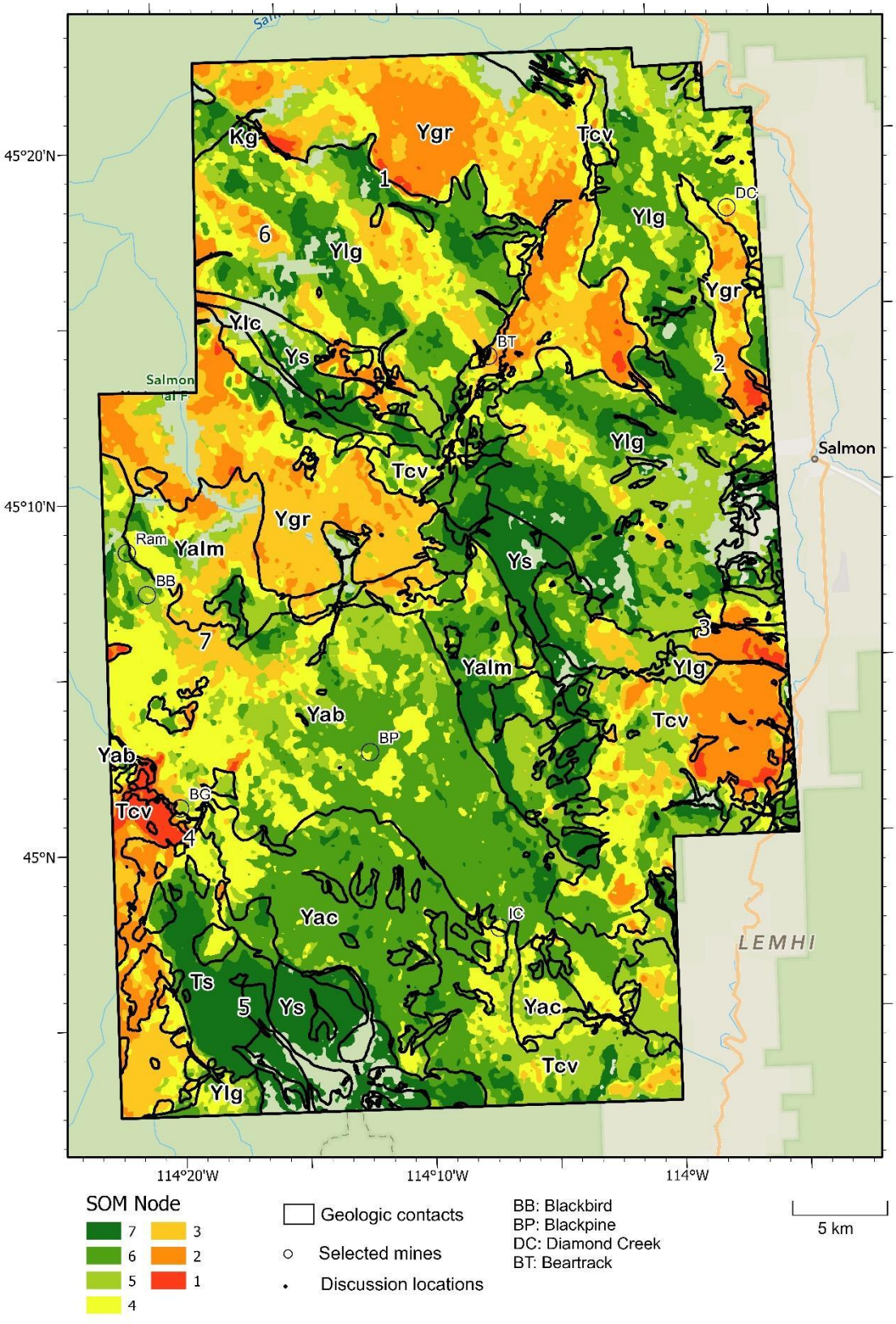

Figure 3.10 Resultant image from Kohonen self-organizing map clustering with seven nodes.

Combinations of techniques

Based on a qualitative visual assessment of the results, the results of the self-organizing map clustering of the principal components most closely matched the mapped geology. Figure 3.11 below represents the first principal component of the potassium, uranium, and thorium dimensions organized into seven self-organizing map (SOM) nodes with the addition of the geologic contacts and selected mine locations. The SOM of the first principal component was more accurate at distinguishing the contact between the Mesoproterozoic granite and Belt Supergroup units than the SOM or k-means clustering of the original data dimensions. The Swauger Formation is delineated well by cluster 1. Clusters five, six, and seven are largely representative of the extrusive and intrusive igneous rocks. Clusters one, two, and three are largely representative of the metasedimentary rocks. Cluster four encompasses both igneous and medasedimentary rocks. The improvement in accuracy can be seen at locations one and two of Figure 3.11, where the clusters associated with the igneous rocks more closely match the mapped location of the contact between granite and Lemhi Group than in the other analyses. In many areas, the results of the SOM of the first principal component are closely equivalent to those of the other statistical techniques. At the location of the Diamond Creek rare earth element deposit, the Lemhi Group is classified as cluster five.

Regional-scale swaths of values representative of the igneous rocks can be seen within the Lemhi Group at locations three, and four, and five. These regional-scale swaths are prime examples of areas for which the statistical analyses of the airborne gamma radiation survey prompt further investigation of the geologic framework. In the vicinity of location five, Evans and Green (2003) mapped several small areas as Hoodoo Formation, which is equivalent to the Swauger Formation in the IGS nomenclature. IGS investigation of these areas in the summer of 2022 determined the presence of bleached quartzite outcrops more likely to be altered Lemhi Group than Swauger Formation. However, at the time of investigation the presence of the regional scale anomalous swaths was not known. Further field work is required to understand these phenomena

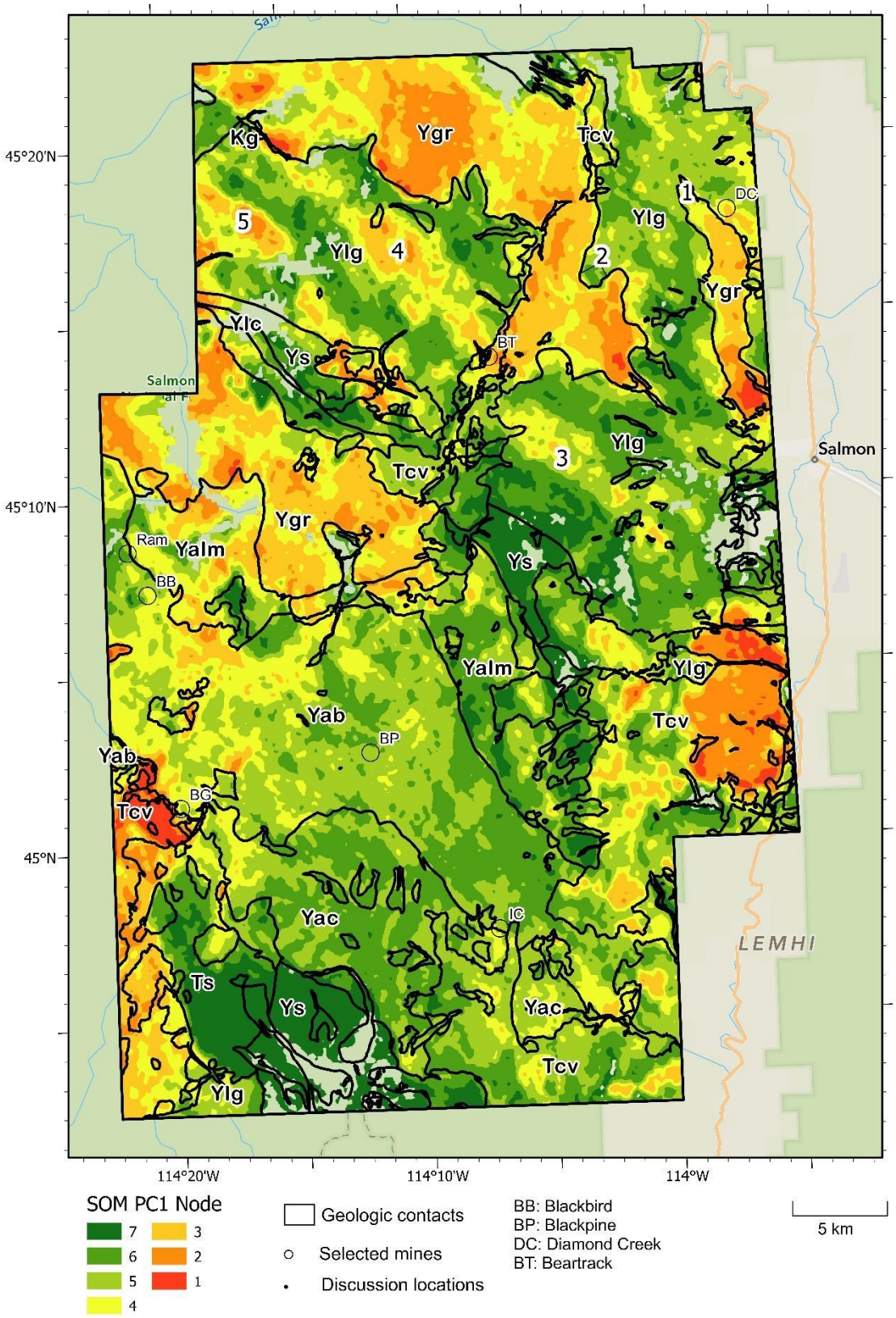

Figure 3.11 Kohonen self-organizing map clustering of first principal component.

Band ratios

Potassium/Thorium

Band ratios have the advantage of diminishing the variable effects of topographic relief, overburden, and vegetative cover. For example, a topographic low will cause, if inadequately corrected for, lower measured concentrations of thorium because of the signal attenuating with distance. Computing the ratio between potassium and thorium will largely negate this topographic effect. Additionally, changes in the potassium to thorium ratio from normal lithologic values may represent potassic alteration, as thorium is typically less mobile than potassium. Potassic alteration may be associated with mineralization (e.g., Shives, 1995).

Several potentially important features can be seen in the band ratio of potassium to thorium. Although some features are readily explained by their spatial association with mapped geology, for other features possible explanations are less apparent. Near the Blackbird and Ram deposits are two strongly juxtaposed bodies of high and low potassium to thorium values within the Lake Mountain and banded siltite members. The body of low potassium to thorium values (Figure 3.12, location one) may represent elevated thorium values from monazite films from contact alteration from the nearby intrusion of granite. To the north across the contact with the Lake Mountain member the granite consistently shows similarly low values. Within the body of high potassium to thorium ratios (location two) Idaho Geological Survey personnel report large amounts of biotite (R. Lewis, personal commun., 2023). This biotite may be a product of potassic alteration. The cause(s) of these opposite extremes in potassium to thorium values is unknown; however, their proximity to the Blackbird and Ram deposits, as well as numerous smaller mines and prospects such as the Beliel Group, suggests that these anomalies warrant further investigation. Additionally, similar zones of strongly juxtaposed values within areas mapped as Belt Supergroup, such as location three, warrant field investigation of possible potassic alteration that may be related to mineralization.

Areas for which high or low values in the potassium to thorium ratio may be explained by the mapped lithology include intrusive syenites and extrusive Challis tuffs. Both the Deep Creek and Arnett Creek syenites can be seen as high values of potassium to thorium (locations four and five). The tuff of Castle Rock is represented by high values of potassium to thorium (location six). Similarly, a large rhyolite dike north of the tuff of Castle Rock is represented by high values of potassium to thorium (location seven).

The Diamond Creek rare earth element deposit can clearly be seen as two small bull's-eyes of low potassium to thorium values (location eight). The northern of the two bull's eyes is at the location described by Anderson (1958) as the Contact claim group and the southern at the location described as the Lucky claim group. The Diamond Creek rare earth element deposit is located within the Lemhi Group and is immediately north of an elongated body of granite. Lows in the potassium to thorium ratio at this location may be a result of high concentrations of monazite at the deposit (Anderson, 1958). Within this general area are several other areas of low potassium to thorium values within the Lemhi Group and in proximity to the Mesoproterozoic granite. Based on the original potassium and thorium gamma radiometric data. Based on the original potassium and thorium gamma radiometric data, some of these low potassium to thorium values represent low concentrations of potassium rather than high concentrations of thorium, such as location 9. Locations ten through thirteen warrant field investigation for the possible presence of alteration and mineralization.

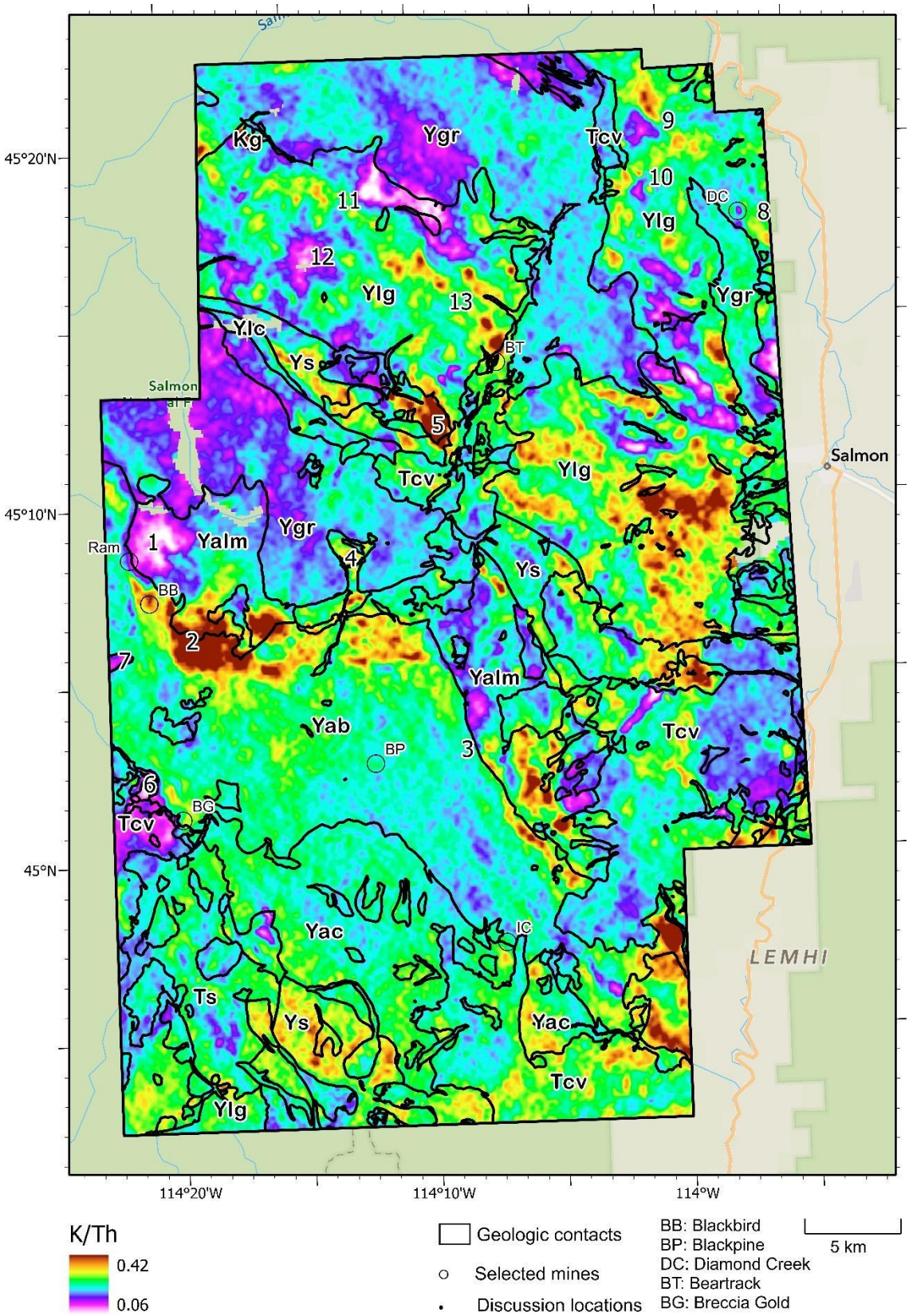

Figure 3.12 Standard deviation stretched (n=3) image representing the potassium to thorium ratio for each cell.

Effimov factor

Within the study area there are multiple zones that are relatively elevated in the Effimov factor. According to Gnojek and Prichystal (1985), values of as much as 1.2 can occur in non-altered rocks, and values greater than 2 suggest alteration. No values in the study area exceed 1; however, the areas of higher values may still warrant further investigation. The Effimov factor values for the study area can be seen below in Figure 3.13.

Immediately north of the mouth of Porphyry Creek is an area (Figure 3.13, location one) with the highest Effimov factor in the study area, with values of approximately 0.95. These values may represent the epithermal system described by Brewer (2020) as the Breccia Gold property of Porphyry Ridge. Alternatively, these values may instead be a product of relatively high uranium values in the tuff of Castle Rock. However, the high values extend outside of the area mapped as the tuff of Castle Rock into the banded siltite member of the Apple Creek Formation.

Towards the northwest corner of the study area along Pine Creek near the contact of the Mesoproterozoic granite and Lemhi Group (location two) is an area with Effimov factor values of approximately 0.77. This area is mapped as granite with minor Quaternary alluvium. An explanation for these high values is not apparent; however, Umpleby (1913) reports a small lead mine in the vicinity. To the northwest of the Beartrack mine there is a swath of elevated Effimov factor values approximately connecting the Beartrack mine to the high Effimov factor value at location two. This same swath can be seen in the clustering analyses and in the potassium to thorium band ratio. The swath may continue southeasterly with dextral offset across the Coiner fault.

Near the locations of the Blackbird and Iron Creek deposits Effimov factor values are slightly elevated (locations three and four, respectively).

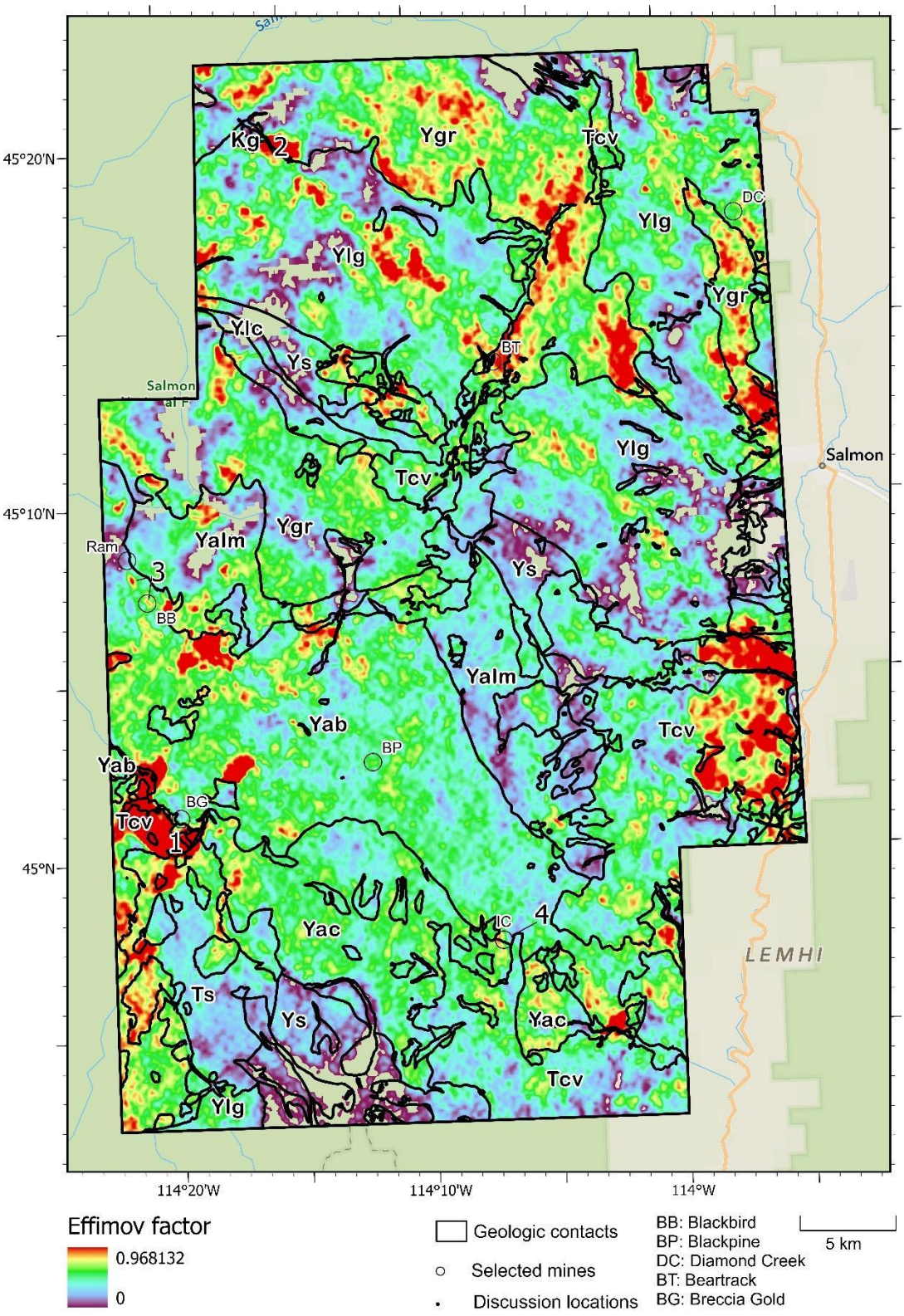

Figure 3.13 Standard deviation stretched (n=3) image of Effimov factor.

Chapter 4: Conclusion

The results of the analyses of the airborne gamma radiation survey, including k-means clustering, principal component analysis, Kohonen self-organizing maps, and clustering of the principal component analysis largely matched the locations of mapped contacts between igneous and metasedimentary rocks. A key limitation of this study was the inability to distinguish the Belt Supergroup units, except for the Swauger Formation. Whereas the Swauger Formation is radiometrically distinct, the rest of the Belt units are radiometrically similar. As a result, efforts to distinguish Belt units based on statistical differences in gamma radiation are hampered. The clusters associated with the coarse siltite and banded siltite include both units indiscriminately. Of the statistical analyses, clustering the first principal component using the Kohonen self-organizing map algorithm most accurately matched the mapped geologic contacts. The potassium to thorium band ratio and self-organizing map of the first principal component identified both known mineral deposits and areas which warrant further investigation for the possibility of mineralization. The results of this study provide valuable information regarding the application of airborne gamma radiation data to differentiate the regional geology of the Salmon River Mountains, such as the ability of the airborne gamma radiation data to distinguish between areas of igneous rocks and areas of metasedimentary rocks. Recommendations for future work include field work in areas identified from the analyses as significantly discordant with the mapped geology (Figure 4.1).

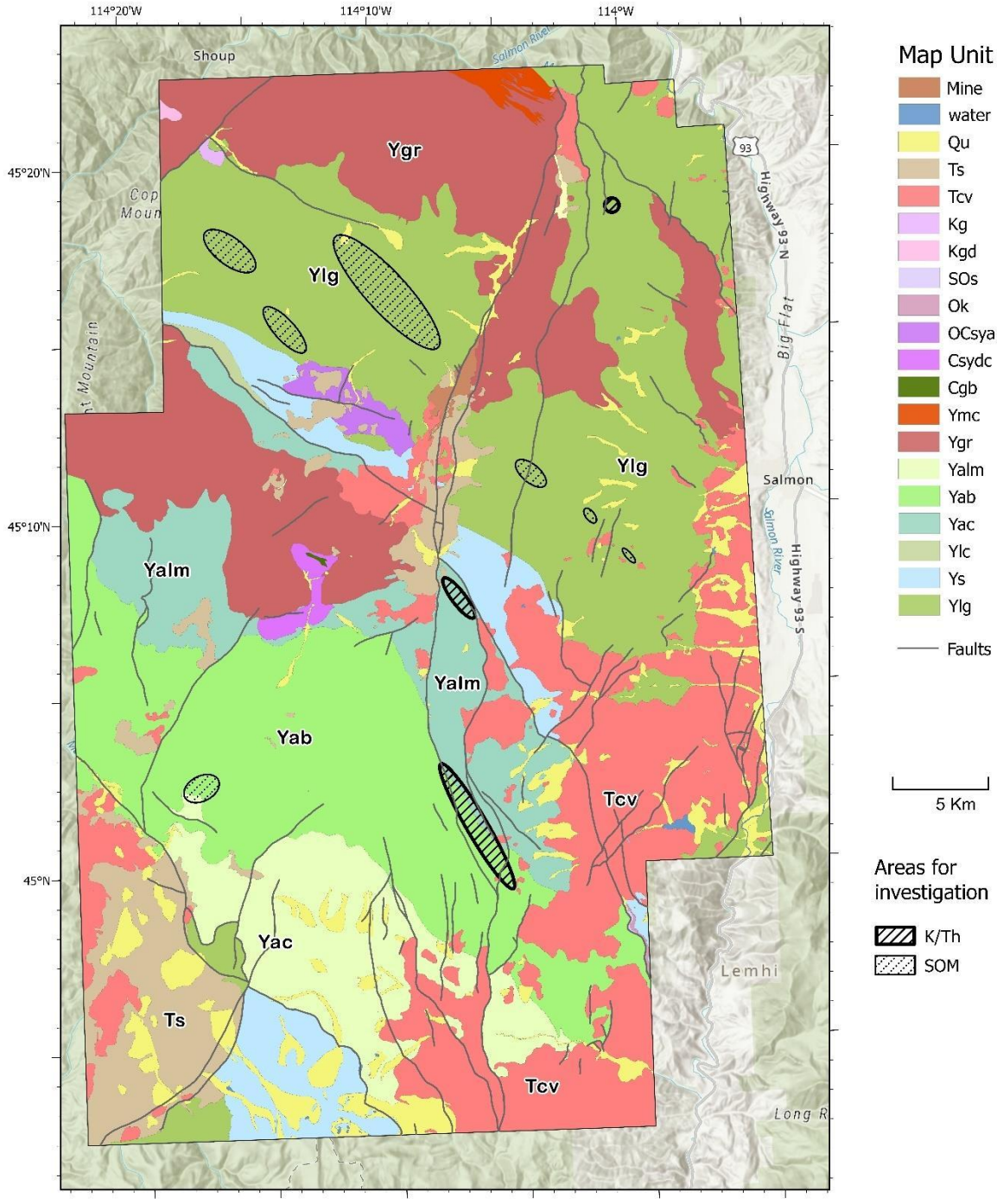

Figure 4.1: Areas recommended for further investigation.

References

Anderson, A.L., 1947, Cobalt mineralization in the Blackbird district, Lemhi County, Idaho: Economic Geology, v. 42, p. 22-46.

Anderson, A.L., 1958, Uranium, thorium, columbium, and rare earth deposits in the Salmon region, Lemhi County, Idaho: Idaho Bureau of Mines and Geology Pamphlet 115, 81 p.

Beartrack-Arnett, 2020, Revival Gold Inc, https://revival-gold.com/beartrack-arnett-gold-project/ (accessed January 2023).

Benjamin Leutner, Ned Horning and Jakob Schwalb-Willmann (2022). RStoolbox: Tools for Remote Sensing Data Analysis. R package version 0.3.0. https://CRAN.R-project.org/package=RStoolbox

Bennett, E.H., 1977, Reconnaissance geology and geochemistry of the Blackbird Mountain-Panther Creek region, Lemhi County, Idaho: Idaho Bureau of Mines and Geology Pamphlet 167, 107 p.

Bennett, E.H., 1986, Relationship of the trans-Challis fault system in central Idaho to Eocene and Basin and Range extensions: Geology, vol. 14, Issue 6, p.481.

Blackpine cobalt-copper project – Koba resources limited Kobaresources.com, https://kobaresources.com/projects/idaho-cobalt-belt/blackpine-project/ (accessed February 2023).

Bookstrom, A.A., 2013, The Idaho cobalt belt: Northwest Geology, v. 42, p. 149–162.

Brewer, B., 2020, Technical Report on the Breccia Gold Property, Southwest of Salmon, Idaho, USA, https://www.ophirgoldcorp.com/_files/ugd/302b27_795ca1239fa6443aa38e2812f9cc75d9.pdf (accessed February 2023).

Burmester, R.F., Lewis, R.S., Othberg, K.L., Stanford, L.R., McFaddan, M.D., and Lonn, J.D., 2012, Geologic map of the Bird Creek quadrangle, Lemhi County, Idaho: Idaho Geological Survey Digital Web Map 153, scale 1:24,000.

Burmester, R.F., Lonn, J.D., Lewis, R.S., and McFaddan, M.D., 2016, Stratigraphy of the Lemhi subbasin of the Belt Supergroup, *in* Maclean, J.S., and Sears, J.W., eds., Belt Basin: Window to Mesoproterozoic Earth: Geological Society of America Special Paper 522, p. 121-137, doi: 10.1130/2016.2522(05).

Carneiro, C. de C., Fraster, S.J., Crósta, A.P., and Silva, A., 2012, Semiautomated geologic mapping using self-organizing maps and airborne geophysics in the Brazilian Amazon: Geophysics, v. 77, doi: 10.1190/geo2011-0302.1.

Carter-McAuslan, A., and Farquharson, C., 2021, Predictive geologic mapping from geophysical data using self-organizing maps: A case study from Baie Verte, Newfoundland, Canada: Geophysics, v. 86, p. B249–B264, doi:10.1190/geo2020-0756.1.

Crocker, B., 2023, Jervois suspends final construction at Idaho Cobalt Operations: Jervoisglobal.com, https://jervoisglobal.com/.

Day, W.C., 2019, The Earth Mapping Resources Initiative (Earth MRI)— Mapping the nation's critical mineral resources (ver. 1.1, March 2019): U.S. Geological Survey Fact Sheet 2019–3007, 2 p., doi: 10.3133/fs20193007.

Dickson, B.L. and Scott, K.M., 1997, Interpretation of aerial gamma-ray surveys - adding the geochemical factors: Australian Geological Survey Organization Journal of Australian Geophysics, v. 17, no.2, p.187-200.

Esri Inc., 2022, ArcGIS Pro 3.0.0.

Evans, K.V., and Green, G.N., 2003, Geologic map of the Salmon National Forest and vicinity, east-central Idaho: U.S. Geological Survey Geologic Investigations Series Map I-2765, scale 1:100,000, 2 sheets, 20 p. text, doi:10.3133/i2765.

Gnojek, I., and Přichystal, A., 1985, A new zinc mineralization detected by airborne gamma-ray spectrometry in northern Moravia (Czechoslovakia): Geoexploration, v. 23, p. 491–502, doi:10.1016/0016-7142(85)90076-6.

Hansen, C.M., and Pearson, D.M., 2016, Geologic map of the Poison Creek thrust fault and vicinity near Poison Peak and Twin Peaks, Lemhi County, Idaho: Idaho Geological Survey Technical Report T-16-1, scale: 1:24,000.

Harris, J.R., Neily, L., Pultz, T., and Slaney, V.R., 1987, Principal component analysis of airborne geophysical data for lithologic discrimination using an image analysis system: Remote Sensing of Environment, v. 2, p. 641–657.

Idaho Cobalt Operations Jervois, https://jervoisglobal.com/projects/idaho-cobalt-operations/ (accessed January 2023).

Idaho Geological Survey - Mines and Prospects Database. Idahogeology.org, https://www.idahogeology.org/geologic-resources/mines-minerals/introduction-to-mines-and-prospects-database (accessed January 2023).

Idaho Strategic Resources, 2023, Diamond Creek: Idaho Strategic Resources Inc, https://idahostrategic.com/diamond-creek-project/ (accessed April 2023).

International Atomic Energy Agency (IAEA), 2003, Guidelines for radioelement mapping using gamma ray spectrometry data: IAEA-TEC-DOC-1363, International Atomic Energy Agency (IAEA), Vienna, 179 p.

Lewis, R.S., Burmester, R.F., and Lonn, J.D., 2019, Geologic map of the Ulysses Mountain quadrangle, Lemhi County, Idaho: Idaho Geological Survey Digital Web Map 188, scale 1:24,000.

Lewis, R.S., Burmester, R.F., Stewart, D.E., and Canada, A.S., 2021a, Geologic map of the Cobalt quadrangle, Lemhi County, Idaho: Idaho Geological Survey Digital Web Map 199, scale 1:24,000.

Lewis, R.S., Canada, A.S., Stewart, D.E., and Burmester, R.F., 2021b, Geologic map of the Degan Mountain quadrangle, Lemhi County, Idaho: Idaho Geological Survey Digital Web Map 200, scale 1:24,000.

Lewis, R.S., and Myers, M.L., 2012, Uranium and additional whole-rock data from the 1976-1980 Challis and Hailey NURE projects, central Idaho: Idaho Geological Survey Digital Analytical Data 7.

Lewis, R.S., Othberg, K.L., Burmester, R.F., Stanford, L.R., McFaddan, M.D., and Lonn, J.D., 2012, Geologic map of the Salmon quadrangle, Lemhi County, Idaho: Idaho Geological Survey Digital Web Map 154, scale 1:24,000.

Lewis, R.S., Othberg, K.L., McFaddan, M.D., Burmester, R.F., Stewart, D.E., Stanford, L.R., and Stewart, E.D., 2013, Geologic map of the Williams Lake quadrangle, Lemhi County, Idaho: Idaho Geological Survey Digital Web Map 162, scale 1:24,000.

Lewis, R.S., Stewart, D.E., Burmester, R.F., Tkach, M.K., and Canada, A.S., 2022, Geologic Map of the Jureano Mountain and Leesburg quadrangles, Lemhi County, Idaho: Idaho Geological Survey Digital Web Map 207, scale 1:24,000.

Lund, K., Tysdal, R.G., Evans, K.V., Kunk, M.J., and Pillers, R.M., 2011, Structural controls and evolution of gold-, silver-, and REE-bearing copper cobalt ore deposits, Blackbird district, east-central Idaho—Epigenetic origins: Economic Geology and the Bulletin of the Society of Economic Geologists, v. 106, p. 585–618, doi:10.2113/econgeo.106.4.585.

Nash, J.T., and Hahn, G.A., 1989, Stratabound Co-Cu deposits and mafic volcaniclastic rocks in the Blackbird mining district, Lemhi County, Idaho, in Boyle, R.W., Brown, A.C., Jefferson, C.W., Jowett, E.C., and Kirkham, R.V., eds., Sediment-Hosted Concordant Copper Deposits: Geological Association of Canada Special Paper 36, p. 339–356.

Phelps, G.A., 2022, Airborne magnetic and radiometric survey, Idaho Cobalt Belt, Central Idaho, 2021 - Magnetic and Radiometric Data: U.S. Geological Survey data release, doi: 10.5066/P9TLBM4U.

Perron, M., Beauvais, M.R., and Kinnan, E., 2023, NI 43-101 Technical Report and Mineral Resource Estimate for the Iron Creek Cobalt-Copper Property, Lemhi County, Idaho, USA.

Ranjbar, H., Hassanzadeh, H., Torabi, M., and Ilaghi, O., 2001, Integration and analysis of airborne geophysical data of the Darrehzar area, Kerman Province, Iran, using principal component analysis: Journal of Applied Geophysics, v. 48, p. 33–41, doi:10.1016/s0926-9851(01)00059-3.

R Core Team (2022). R: A language and environment for statistical computing. R Foundation for Statistical Computing, Vienna, Austria. https://www.R-project.org/.

Robert J. Hijmans (2022). raster: Geographic Data Analysis and Modeling. R package version 3.5-29. https://CRAN.R-project.org/package=raster.

Roger Bivand, Tim Keitt and Barry Rowlingson (2022). rgdal: Bindings for the 'Geospatial' Data Abstraction Library. R package version 1.5-32. https://CRAN.R-project.org/package=rgdal.

Shives, R.B.K., Charbonneau, B.W., and Ford, K.L., 2000, The detection of potassic alteration by gamma-ray spectrometry—Recognition of alteration related to mineralization: Geophysics, v. 65, p. 2001–2011, doi:10.1190/1.1444884.

Schulz, K.J., DeYoung, J.H., Jr., Bradley, D.C., and Seal, R.R., II, 2017, Critical mineral resources of the United States—An introduction, chap. A of Schulz, K.J., DeYoung, J.H., Jr., Seal, R.R., II, and Bradley, D.C., eds., Critical mineral resources of the United States—Economic and environmental geology and prospects for future supply: U.S. Geological Survey Professional Paper 1802, p. A1–A14, doi.org:10.3133/pp1802A.

Slack, J.F., 2012, Stratabound Fe-Cu-Co-Au-Bi-Y-REE deposits of the Idaho cobalt belt, USA: Multistage hydrothermal mineralization in a magmaticrelated iron oxide-copper-gold system: Economic Geology and the Bulletin of the Society of Economic Geologists, v. 107, p. 1089–1113, doi:10.2113/econgeo.107.6.1089.

Staatz, M.H., Sharp, B.J., and Hetland, D.L., 1979, Geology and mineral resources of the Lemhi Pass thorium district, Idaho and Montana, with a section on description of selected thorium veins: U.S. Geological Survey Circular 805, 46 p. doi:10.3133/pp1049a.

Stewart, D.E., Canada, A.S., Burmester, R.F., and Lewis, R.S., 2021, Geologic map of the Taylor Mountain quadrangle, Lemhi County, Idaho: Idaho Geological Survey Digital Web Map 201, scale 1:24,000.

Umpleby, J.B., 1913, Geology and ore deposits of Lemhi County, Idaho: U.S. Geological Survey Bulletin 528, 182 p.

U.S. Geological Survey, 2022a, List of critical minerals: https://www.usgs.gov/news/national-news-release/us-geological-survey-releases-2022-list-critical-minerals.

Vhay, J.S., 1948, Copper-cobalt deposits of the Blackbird district, Lemhi County, Idaho. U.S. Geological Survey Strategic Minerals Investigations Preliminary Report 3–219, 26 p.

Wang, C., Slack, J.F., Shah, A.K., Yates, M.G., Lentz, D.R., Whittaker, A.T.H., and Marvinney, R.G., 2023, A recently discovered trachyte-hosted rare earth element-niobium-zirconium occurrence in northern Maine, USA: Economic geology and the bulletin of the Society of Economic Geologists, v. 118, p. 1–13, doi:10.5382/econgeo.4993.

Wehrens R., and Kruisselbrink, J., 2018, Flexible Self-Organizing Maps in Kohonen 3.0., Journal of Statistical Software, *87*(7), 1-18. doi: 10.18637/jss.v087.i07

Weihermann, J. D., Ferreira, M. P., Ferreira, F. J. F., and Silva, A. M., 2020, Using Unsupervised Clustering for Analyzing Airborne Gamma-Ray Spectrometry Data: IGARSS 2020 - 2020 IEEE International Geoscience and Remote Sensing Symposium, doi: 10.1109/igarss39084.2020.9323223.